Disentangling superconducting and magnetic orders in NaFe_{1−x}Ni_{x}As using muon spin rotation

Sky C. Cheung *et al.*

Phys. Rev. B **97**, 224508 — Published 12 June 2018

DOI: 10.1103/PhysRevB.97.224508

Disentangling superconducting and magnetic orders in $NaFe_{1-x}Ni_xAs$ using muon spin rotation

Sky C. Cheung,[1,*] Zurab Guguchia,[1,*] Benjamin A. Frandsen,[1] Zizhou Gong,[1] Kohtaro Yamakawa,[1] Dalson E. Almeida,[2] Ifeanyi J. Onuorah,[3] Pietro Bonfá,[4] Eduardo Miranda,[5] Weiyi Wang,[6] David W. Tam,[6] Yu Song,[6] Chongde Cao,[6,7] Yipeng Cai,[8] Alannah M. Hallas,[8] Murray N. Wilson,[8] Timothy J.S. Munsie,[8] Graeme Luke,[8,9,10] Bijuan Chen,[11] Guangyang Dai,[11] Changqing Jin,[11] Shengli Guo,[12] Fanlong Ning,[12] Rafael M. Fernandes,[13] Roberto De Renzi,[3] Pengcheng Dai,[6] and Yasutomo J. Uemura[1,†]

[1] *Department of Physics, Columbia University, New York, NY 10027 USA*
[2] *UEMG Unidade Passos, Av. Juca Stockler, 1130, CEP 37900-106 Passos, MG, Brazil*
[3] *Department of Mathematical, Physical and Computer Sciences, Parco delle Scienze 7A, I-43124 Parma, Italy*
[4] *CINECA, Casalecchio di Reno 6/3 40033 Bologna, Italy*
[5] *Instituto de Física Gleb Wataghin, Unicamp, Rua Sérgio Buarque de Holanda, 777, CEP 13083-859 Campinas, SP, Brazil*
[6] *Department of Physics and Astronomy, Rice University, Houston, Texas 77005, USA*
[7] *Department of Applied Physics, Northwestern Polytechnical University, Xian 710072, China*
[8] *Department of Physics and Astronomy, McMaster University, Hamilton, ON L8S 4M1 Canada*
[9] *Canadian Institute for Advanced Research, Toronto, ON, Canada M5G 1M1*
[10] *TRIUMF, 4004 Wesbrook Mall, Vancouver, B.C., Canada, V6T 2A3*
[11] *Beijing National Laboratory for Condensed Matter Physics; Institute of Physics, Chinese Academy of Sciences; School of Physics, University of Chinese Academy of Sciences, Beijing 100190, China*
[12] *Department of Physics, Zhejiang University, Hangzhou 310027, China*
[13] *School of Physics and Astronomy, University of Minnesota, Minneapolis, Minnesota 55455, USA*

(Dated: April 25, 2018)

Muon spin rotation and relaxation studies have been performed on a "111" family of iron-based superconductors, $NaFe_{1-x}Ni_xAs$, using single crystalline samples with Ni concentrations $x = 0$, 0.4, 0.6, 1.0, 1.3, and 1.5%. Static magnetic order was characterized by obtaining the temperature and doping dependences of the local ordered magnetic moment size and the volume fraction of the magnetically ordered regions. For $x = 0$ and 0.4%, a transition to a nearly-homogeneous long range magnetically ordered state is observed, while for $x \gtrsim 0.4\%$ magnetic order becomes more disordered and is completely suppressed for $x = 1.5\%$. The magnetic volume fraction continuously decreases with increasing x. Development of superconductivity in the full volume is inferred from Meissner shielding results for $x \gtrsim 0.4\%$. The combination of magnetic and superconducting volumes implies that a spatially-overlapping coexistence of magnetism and superconductivity spans a large region of the T-x phase diagram for $NaFe_{1-x}Ni_xAs$. A strong reduction of both the ordered moment size and the volume fraction is observed below the superconducting T_C for $x = 0.6$, 1.0, and 1.3%, in contrast to other iron pnictides in which one of these two parameters exhibits a reduction below T_C, but not both. The suppression of magnetic order is further enhanced with increased Ni doping, leading to a reentrant non-magnetic state below T_C for $x = 1.3\%$. The reentrant behavior indicates an interplay between antiferromagnetism and superconductivity involving competition for the same electrons. These observations are consistent with the sign-changing $s^{\pm}$ superconducting state, which is expected to appear on the verge of microscopic coexistence and phase separation with magnetism. We also present a universal linear relationship between the local ordered moment size and the antiferromagnetic ordering temperature T_N across a variety of iron-based superconductors. We argue that this linear relationship is consistent with an itinerant-electron approach, in which Fermi surface nesting drives antiferromagnetic ordering. In studies of superconducting properties, we find that the $T = 0$ limit of superfluid density follows the linear trend observed in underdoped cuprates when plotted against T_C. This paper also includes a detailed theoretical prediction of the muon stopping sites and provides comparisons with experimental results.

PACS numbers: 74.20.Mn, 74.25.Ha, 74.70.Xa, 76.75.+i
Keywords: Condensed Matter Physics, Strongly Correlated Materials, Superconductivity, Magnetism

I. INTRODUCTION

Iron-based high temperature superconductors (Fe-HTS) are materials exhibiting unconventional superconductivity that arise from parent compounds with static antiferromagnetic (AFM) order[1–3]. One of the grand challenges in understanding the behavior of these systems is determining the physical mechanism responsible for superconductivity. Essential information on the nature of superconductivity in strongly correlated electron systems can be deduced by investigating their phase diagrams as well as the superconducting (SC) gap structure.

In the parent compound of many Fe-HTS, a spin density wave forms with spins ordered antiparallel to

each other along one Fe-Fe axis and parallel to each other along the orthogonal Fe-Fe bond direction[1,2,4]. Carrier doping, isovalent chemical substitution, or application of pressure to the parent system suppresses magnetic order and begets a SC dome[5]. In addition to magnetism and superconductivity, Fe-HTS exhibit a tetragonal-to-orthorhombic structural distortion at a temperature T_S that precedes or occurs concurrently with the magnetic phase transition at temperature T_N[1,3,4,6,7]. The prominent in-plane anisotropy in resistivity along orthogonal axes in the paramagnetic (PM) orthorhombic state is associated with an electronic nematic order parameter that triggers the orthorhombic distortion of the crystal[8,9]. The aforementioned orders are found in close proximity with each other. AFM and SC orders homogeneously coexist in several Fe-HTS, such as in $BaFe_{2-x}Co_xAs_2$[10,11], $BaFe_{2-x}Ni_xAs_2$[12], $Ba_{1-x}K_xFe_2As_2$[13] , and $NaFe_{1-x}Co_xAs$[14] . In these systems, the ordered magnetic moment size and nematic order parameter smoothly decrease as the temperature is lowered below T_C, corroborating the fact that superconductivity and magnetic long range order compete for the same electrons[15]. However, other studies[16,17] have detected the mutual exclusion of these two order parameters, i.e. they exhibit macroscopic phase separation in different parts of the sample. Characterizing common features of the complex interplay among magnetic, nematic, and SC orders in various Fe-HTS is essential for elucidating the microscopic pairing mechanism in Fe-HTS and other unconventional superconductors.

One of the major experimental challenges in teasing apart AFM and SC orders is that individual experimental probes have limited ranges of sensitivity to magnetism and/or superconductivity. For instance, neutron scattering and magnetic susceptibility measurements can only reveal volume-integrated information about the magnetic and SC features of the specimens. At present, no individual experimental probe can unambiguously address the issue of whether the coexistence of AFM and SC orders directly overlap in real space or if the specimen undergoes macroscopic phase separation between two phases. In an attempt to clear this experimental hurdle, a detailed multiple-probe investigation was recently conducted on $BaFe_{2-x}Ni_xAs_2$, involving Muon Spin Rotation (μSR), Scanning Tunneling Microscopy (STM), Mössbauer spectroscopy, neutron scattering, and specific heat measurements[12]. The results from this study offer convincing evidence that the AFM and SC phases in $BaFe_{2-x}Ni_xAs_2$ almost completely overlap in real space and both phases compete for the same electrons. The question of whether a similar style of phase coexistence exists in other families of Fe-HTS remains unclear. In this work, we present a detailed μSR investigation in context with recent susceptibility and neutron scattering measurements to gain a deeper understanding of the interplay between AFM and SC orders in $NaFe_{1-x}Ni_xAs$, a member of the "111" family of Fe-HTS.

Recent neutron scattering experiments on $NaFe_{1-x}Ni_xAs$ show that the neutron magnetic order parameter is diminished below T_C[18], which was interpreted as the reduction of the magnetic moment below T_C. Using the volume sensitive μSR technique, we demonstrate for the first time in single crystalline samples of $NaFe_{1-x}Ni_xAs$, with $x = 0.6$, 1.0, 1.3, and 1.5%, that the reduction of magnetic intensity is due to a strong reduction of *both* the ordered moment and the magnetic volume fraction below T_C. The debilitating effect of superconductivity on magnetism intensifies as the doping level x increases, leading to a reentrant non-AFM state below T_C for $x = 1.3\%$. These results suggest an interesting scenario, in which the degree of competition between AFM and SC may be itself intrinsically inhomogeneous, varying as a function of position in the sample. Moreover, we establish a robust linear dependence between the ordered moment and the AFM ordering temperature T_N for various Fe-HTS, which is consistent with a model of itinerant magnetism in Fe-HTS.

This work is organized as follows: Section II describes the preparation and handling of the specimens, dc-susceptibility characterization, and the μSR experimental setup. Experimental zero-field μSR results are shown in Section III A and compared with neutron scattering results in Section III B. A discussion of these results is presented in Section III C. Section IV introduces a muon stopping site simulation performed to account for the multiple internal magnetic fields observed in the zero-field μSR spectra. Knowledge of the muon site locations enables the ordered moment size to be determined from the observed precession frequency. Section V describes a universal linear relation between the ordered moment size and T_N. A theoretical discussion of this result using a model of antiferromagnetism in Fe-HTS parent compounds based on an itinerant electron picture is also presented in this section. Section VI shows μSR measurements under a transverse external field on superconducting $NaFe_{1-x}Ni_xAs$ and demonstrates that a linear relationship between the superfluid density and T_C is observed in $NaFe_{1-x}Ni_xAs$ and other high-T_C cuprate superconductors. These results are summarized in the concluding Section VII. Appendix A describes detailed methods and results of the internal field simulation. A calculation for the universal scaling of the ordered moment size and ordering temperature based on a two-band model is presented in Appendix B. Finally, Appendix C provides a derivation of the superconducting gap symmetry from the temperature dependence of the penetration depth.

II. EXPERIMENTAL METHODS

Pristine single-crystal specimens of $NaFe_{1-x}Ni_xAs$ with $x = 0$, 0.4, 0.6, 0.8, 1.0, 1.3 and 1.5% were prepared using the self-flux technique in accordance with Ref. 21, with each crystallite measuring about $1 \times 1 \times 0.2$

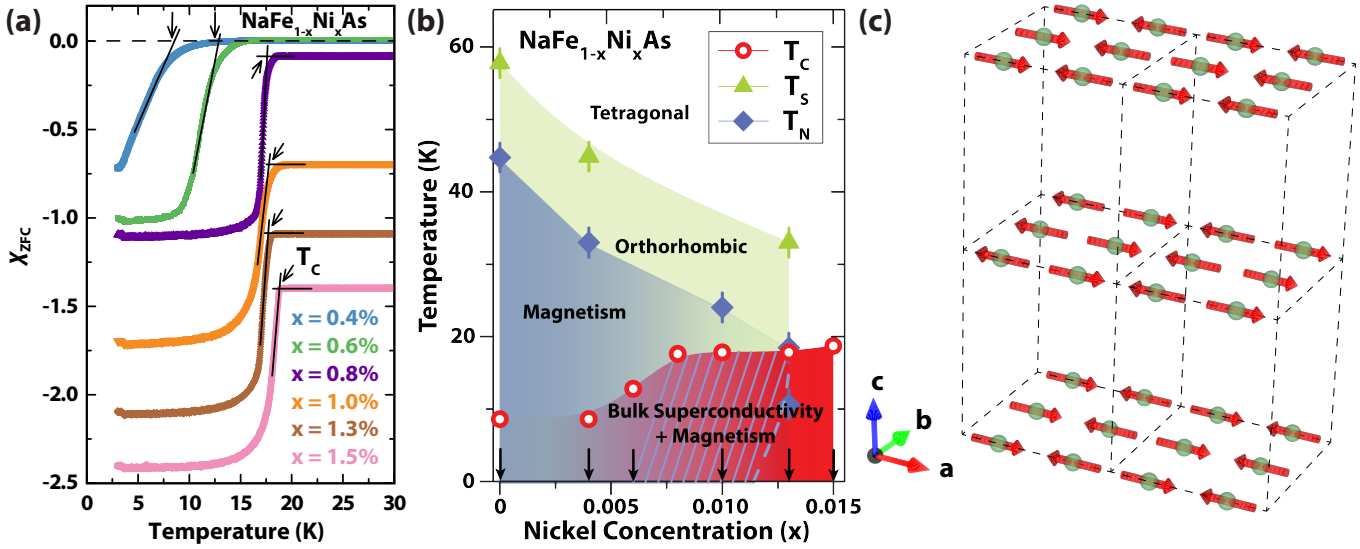

FIG. 1. Magnetic characterization of $NaFe_{1-x}Ni_xAs$. (a) Temperature-dependent DC susceptibility measurements in a magnetic field of 5 Oe applied in the ab plane. Full SC volume is obtained for $x \geq 0.4\%$. Susceptibility spectra for $x \geq 0.8\%$ are vertically offset for visual clarity. Black solid lines show how T_C (indicated by black arrows) was determined for each doping. (b) Phase diagram of $NaFe_{1-x}Ni_xAs$ illustrating temperature and doping dependences of various orders, with structural and magnetic transitions obtained from Ref. 18 and displayed as fully-colored symbols. Superconducting transition temperatures T_C were determined from magnetic susceptibility measurements shown in (a). Black arrows indicate the doping concentrations measured by μSR in our present investigation. (c) Collinear AFM spin structure of the undoped compound NaFeAs[19,20]. Only Fe atoms (green) are shown for visual clarity. Dashed lines indicate the boundaries of a single unit cell of the crystal structure.

mm^3. Zero-field cooling DC susceptibility measurements were performed on these samples in an applied field of 5 Oe in the basal a-b plane down to 3 K and the results are shown in Figure 1(a). These measurements indicate that $NaFe_{1-x}Ni_xAs$ exhibits bulk superconductivity with full SC shielding fraction for the range $x = 0.6 \sim 1.5\%$, with a maximum $T_C \approx 17$ K achieved for $x = 1.5\%$. A phase diagram summarizing the structural, magnetic, and SC transitions is shown in Figure 1(b), which is reminiscent of the electronic phase diagrams of $NaFe_{1-x}Co_xAs$[22,23] and $NaFe_{1-x}Cu_xAs$[24]. For clarity, collinear AFM spin structure of the undoped compound NaFeAs is also shown in Fig. 1(c).

Since $NaFe_{1-x}Ni_xAs$ is highly air and moisture sensitive, the crystallites were tightly encased in packets of Kapton film inside an Ar-filled glovebox. Each crystallite was aligned so that the crystallographic c-axis was oriented normal to the film packet, without any preferred alignment of the basal ab plane. For each doping concentration, packets containing a few large crystal specimens were mounted on an ultra-low background sample holder using aluminum tape.

In a μSR experiment, positive muons implanted into a specimen serve as extremely sensitive local probes to simultaneously measure small internal magnetic fields and ordered magnetic volume fractions. Therefore, we can ascertain the temperature and doping evolution of the magnetic volume fraction and ordered moment separately, unlike reciprocal-space techniques such as neutron scattering. Time differential μSR measurements were performed using the Los Alamos Meson Physics Facility (LAMPF) spectrometer with a helium gas-flow cryostat at the M20 surface muon beamline (500 MeV) of TRIUMF in Vancouver, Canada and using the General Purpose Surface-Muon Instrument (GPS) with a standard low-background veto setup at the πM3 beam line of the Paul Scherrer Institute in Villigen, Switzerland. A continuous beam of 100% spin polarized muons was implanted into the sample and the time dependence of the ensemble muon polarization was collected at temperatures between 2K and 70K. The muon beam momentum was parallel to the crystal c axis. By applying magnetic fields to the muon beam before the sample, the ensemble muon spin prior to implantation can be oriented parallel or perpendicular to the beam direction. See Refs. 25–27 for further details on the μSR experimental technique. The μSR spectra were analyzed in the time domain using least-squares optimization routines from the `musrfit` software suite[28].

III. MAGNETISM IN $NaFe_{1-x}Ni_xAs$

A. Zero Field μSR Results

The observed μSR time spectra (muon ensemble polarization) of $x = 0$, 0.4, 0.6, 1.0, 1.3 and 1.5% in zero applied field (ZF-μSR) are shown in Figure 2. In these mea-

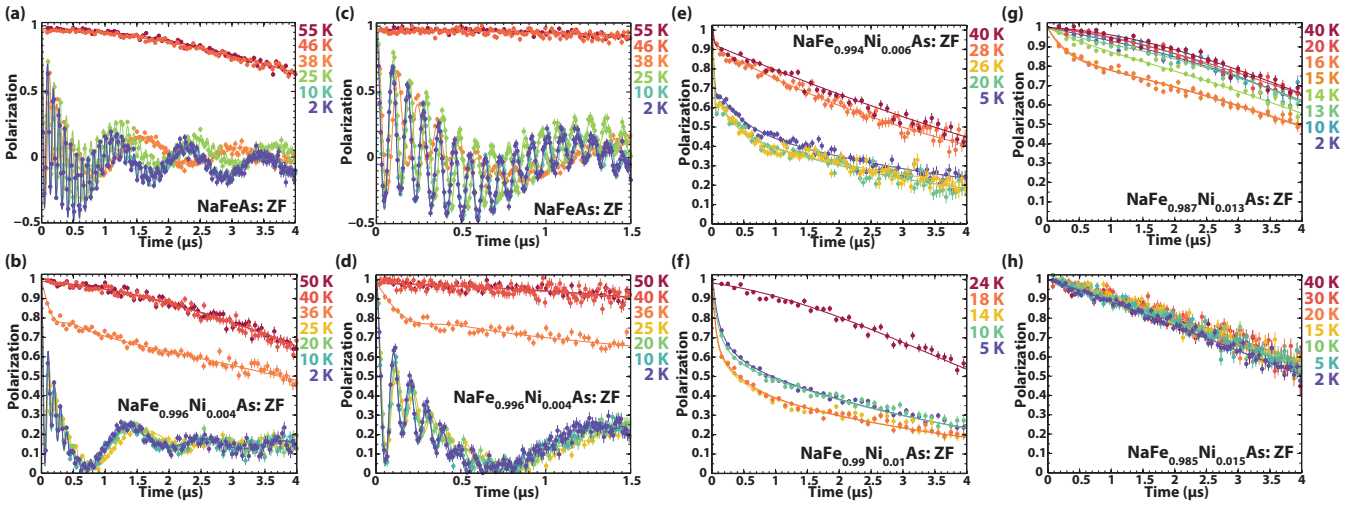

FIG. 2. ZF-μSR spectra on $NaFe_{1-x}Ni_xAs$. (a)-(b) Muon spin polarization in zero field for $NaFe_{1-x}Ni_xAs$ for $x = 0$ and 0.4%, respectively. (c)-(d) Zoomed-in view of the first 1.5 microseconds of the spectra shown in (a) and (b). (e)-(h) Time spectra for the $x = 0.6$, 1.0, 1.3, and 1.5% compound in zero field, respectively. Solid lines in all panels are fits of the data to the ZF-μSR model in (1) for each temperature. Additional details on the μSR time spectra and experimental geometry can be found in Refs. 25–27.

surements, the initial muon spin polarization is in the a-b plane of the crystals, and the time spectra were obtained using up and down positron counters. At high temperatures, only a very faint depolarization of the μSR signal is observed. This weak relaxation mostly originates from the interaction of the muon spin with randomly oriented nuclear magnetic moments. Upon cooling, the relaxation of the μSR signal increases due to the proliferation of Fe-spin correlations.

For $x = 0$ and 0.4% samples, three distinct precession frequencies occur in the μSR spectra, which emanate from three magnetically inequivalent muon stopping sites in $NaFe_{1-x}Ni_xAs$, in agreement with our stopping site calculations presented in Section IV. No coherent oscillations are present in the $x \gtrsim 0.6\%$ spectra shown in Figure 2(e)-(f), even at the lowest measured temperature, as only a rapidly relaxing signal is observed. The fast depolarization of the μSR signal (without oscillations) arises from a broad distribution of static internal magnetic fields, which has been confirmed using longitudinal field (LF)-μSR experiments. These measurements reveal that the muon spin relaxation is substantially suppressed at modest longitudinal external fields between 25 and 50 mT (of the order of internal quasistatic fields), suggesting an inhomogeneous magnetic state in the samples with $x = 0.6$, 1.0 and 1.3%. The ZF-μSR time spectra for the $x = 1.3\%$ compound shown in Figure 2(g) demonstrate magnetic ordering between 14 K and 17 K. Below 14 K, magnetic order vanishes and the specimen only exhibits bulk superconductivity. Interestingly, a similar re-entrance to a non-magnetic state was observed in $BaFe_{2-x}Co_xAs_2$ by neutron diffraction[15]. In the following, we present how the magnetic properties of $NaFe_{1-x}Ni_xAs$ evolve with temperature and doping.

All of the ZF-μSR spectra were fit to the following phenomenological model:

$$P_{\rm ZF}(t) = F\left(\sum_{j=1}^{3}\left(f_j\cos(2\pi\nu_j t+\phi)e^{-\lambda_j t}\right)+f_L e^{-\lambda_L t}\right)+(1-F)\left(\frac{1}{3}+\frac{2}{3}\left(1-\lambda t-(\sigma t)^2\right)e^{-\lambda t-\frac{1}{2}(\sigma t)^2}\right) \quad (1)$$

The model in (1) consists of an anisotropic magnetic contribution characterized by an oscillating "transverse" component and a slowly relaxing "longitudinal" component. The longitudinal component arises due to the parallel orientation of the muon spin polarization and the local magnetic field. In polycrystalline samples with randomly oriented fields this results in a so-called "one-third tail" with $f_L = \frac{1}{3}$. For single crystals, f_L varies between zero and unity as the orientation between field and polarization changes from being parallel to perpendicular. In addition to the magnetically ordered contribution, there is a PM signal component characterized by the densely distributed network of nuclear dipolar moments σ and dilute electronic moments with random orientations λ[29]. The temperature-dependent magnetic ordering fraction $0 \le F \le 1$ governs the trade-off between magnetically-

ordered and PM behaviors.

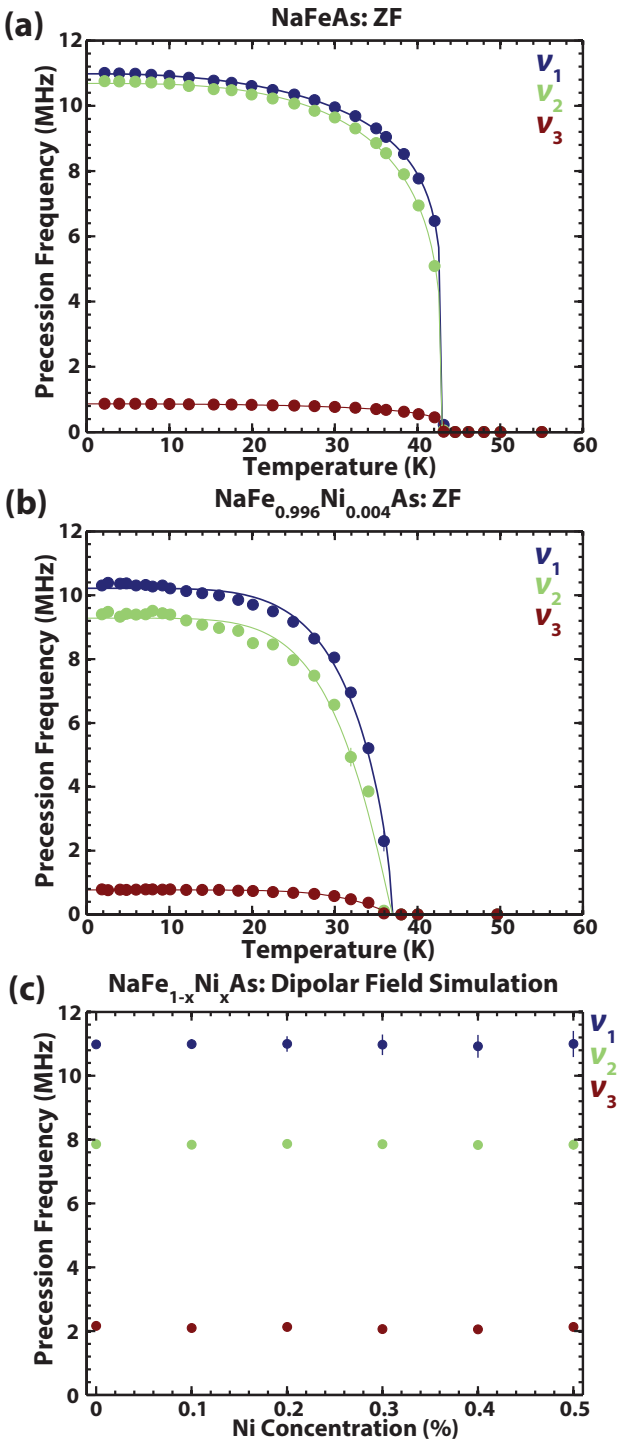

FIG. 3. Muon precession frequencies in $NaFe_{1-x}Ni_xAs$. (a)-(b) Precession frequencies ν_j from the model used in (1) on the $x = 0$ and 0.4% compounds, respectively. Solid lines are power-law fits to the data. (c) Simulation results from dipolar field calculations on lightly-doped $NaFe_{1-x}Ni_xAs$ using the three muon stopping sites obtained from DFT calculations.

Shown in Figure 3(a)-(b) are the temperature dependences of the precession frequencies observed in the $x = 0$ and 0.4% samples. For the undoped and $x = 0.4\%$ systems, there are three distinct frequencies that share the same relationship $\nu(T) = \nu(0)(1 - (\frac{T}{T_N})^a)^b$, which are indicated by solid lines. In the parent system, a sharp step-like increase of $\nu(T)$ is observed below $T_N \approx 42$ K, which may be a signature of a first-order phase transition, although further experiments are needed to establish the character of the transition. This feature is absent in the $x = 0.4\%$ sample, which could be due to disorder effects introduced by Ni impurities[30]. Similar ZF-μSR experiments were also performed by using positron counters located in the forward and backward directions with respect to the muon beam direction. Interestingly, the two fast frequencies are absent in the non-spin-rotated spectra for $x = 0$ and 0.4%. If we associate each frequency to a different muon stopping site, these results suggest that the magnetic field directions at the high-field stopping sites are oriented along c axis of the crystal. This feature is consistent with dipolar field simulations on muon stopping sites presented in Section IV.

We define the static magnetic order parameter $\mathcal{M} \equiv \sqrt{(2\pi\nu)^2 + \lambda_T^2}$ to track the temperature and doping dependence of magnetism, where ν is the maximum precession frequency and λ_T is the relaxation rate corresponding to ν. As defined, $\mathcal{M}$ takes into account both homogeneous (well-defined precession frequency ν) and inhomogeneous contributions (rapid early-time relaxation λ_T) to the signal. Therefore, the magnetic transition temperature T_N corresponds to the onset of $\mathcal{M}$.

The temperature and doping evolution of the magnetic fraction F and magnetic order parameter $\mathcal{M}$ are shown in Figure 4. The relative decrease in $\mathcal{M}$ below T_C is more pronounced with increased doping, as seen in Figure 4(b). Indeed, the $x = 1.3\%$ sample exhibits reentrant behavior in which the low-temperature state becomes non-AFM below T_C within experimental uncertainty. The temperature evolution of the magnetically ordered fraction F is shown in Figure 4(a). F shows a sharp increase below T_N while the onset of SC causes F to decrease when cooled below T_C. With higher doping, a stronger reduction of F is observed below T_C. For the $x = 1.3\%$ system, magnetic order is completely destroyed and the system loses long-range AFM order below 14 K. The evolution of magnetic and SC volume fractions across temperature and doping is presented in Figure 5.

B. Comparison with Elastic Neutron Scattering

Muon spin rotation and neutron scattering are two powerful experimental techniques for studying magnetic materials. As described in Ref. 31, these methods have distinct features that make them complementary probes of magnetism. For instance, both techniques are sensitive to different time scales of dynamic fluctuations. However, since we are probing static magnetic order in $NaFe_{1-x}Ni_xAs$, both μSR and elastic neutron scattering

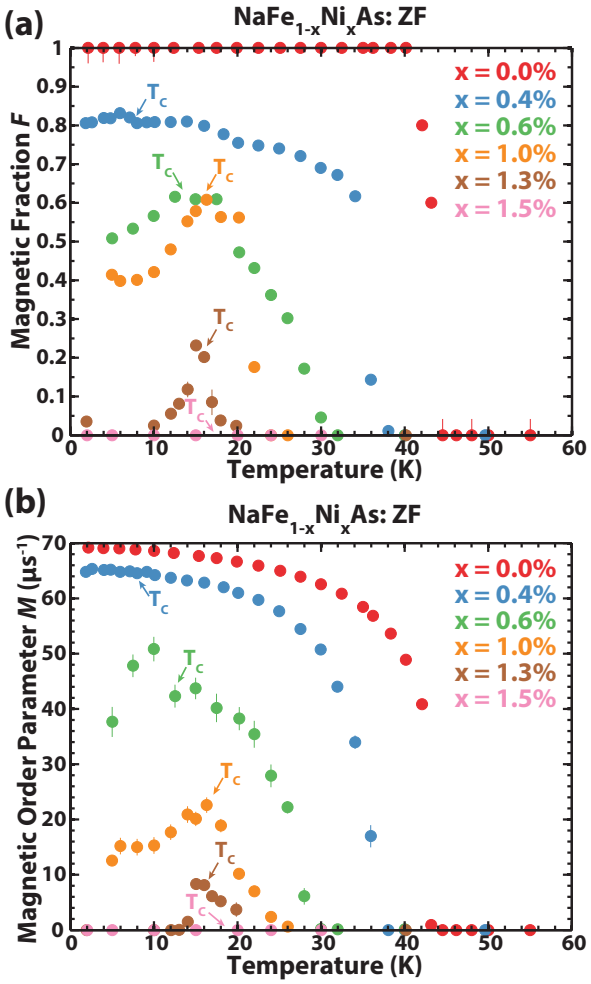

FIG. 4. Summary of ZF-μSR fit results on $NaFe_{1-x}Ni_xAs$. (a) Magnetically ordered volume fraction (F) as a function of temperature and Ni concentration. (b) Static magnetic order parameter ($\mathcal{M}$) as a function of temperature and Ni concentration. Arrows in the figures denote T_C for the various samples.

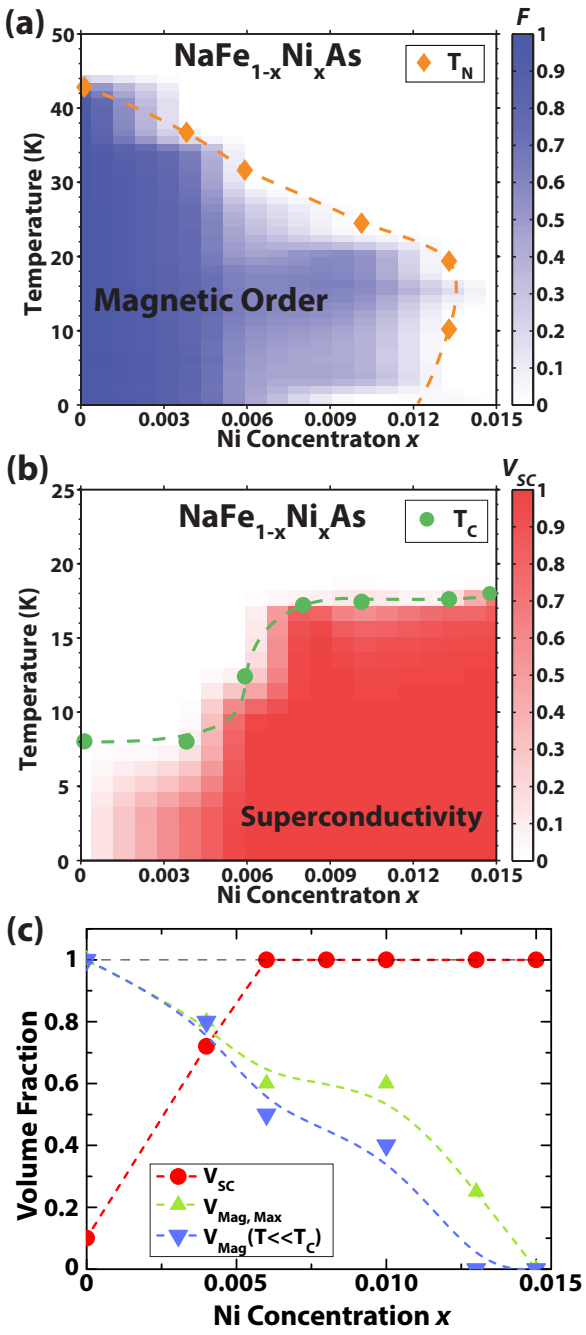

FIG. 5. Magnetic and SC volume fractions in $NaFe_{1-x}Ni_xAs$. (a) Doping and temperature evolution of the magnetic fraction $V_{\rm Mag} = F$ from ZF-μSR. Orange diamonds indicate T_N and the dashed curve is a guide to the eye. Observe the bend in the curve near $x = 0.013$ indicating a reentrant non-AFM phase. (b) Doping and temperature evolution of the SC volume fraction from magnetic susceptibility measurements presented in Figure 1(a). Green circles indicate T_C and the dashed curve is a guide to the eye. (c) Summary of magnetic and SC volume fractions. V_{SC} is the SC volume fraction, $V_{\rm Mag,\ Max}$ is the maximum value of F for each doping, and $V_{\rm Mag}(T \ll T_C)$ is F at temperatures much less than T_C.

should yield consistent results. In addition, as a volume-integrating probe in reciprocal space, neutron scattering is sensitive to both the ordered moment and its volume fraction, but these two contributions cannot be separated from the measured scattered intensity. However, μSR enables independent measurements of both the volume fraction and the ordered moment size, unlike neutron scattering and other bulk probes.

As decsribed in Section I, elastic neutron scattering experiments on $NaFe_{1-x}Ni_xAs$ reveal that the neutron magnetic order parameter is diminished below T_C[18], which was interpreted as the reduction of the magnetic moment below T_C. However, the suppression of magnetic order below T_C observed in neutron diffraction cannot be unambiguously attributed to a reduction of the magnetic moment, as pointed out in the previous paragraph. A comparison between the neutron magnetic order pa-

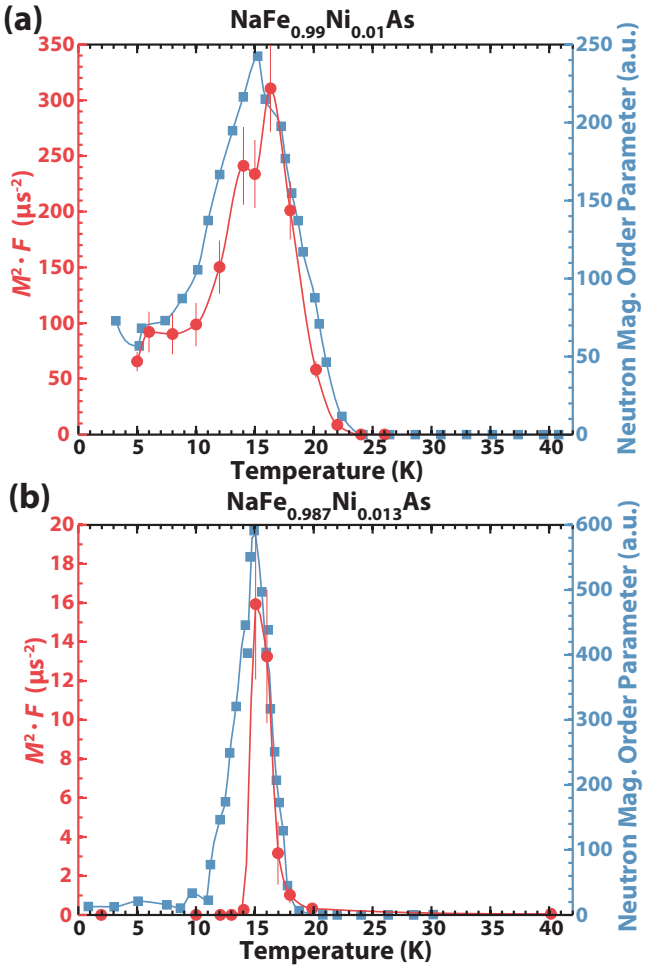

FIG. 6. Comparison of μSR and elastic neutron scattering measurements[18] for the (a) $x = 1.0\%$ and (b) $x = 1.3\%$ compounds. The magnetic strength $\mathcal{M}^2F$ from μSR measurements is plotted in red and the Bragg peak intensity from neutron scattering is shown in blue.

rameter and the magnetic strength $\mathcal{M}^2F$ from our μSR studies is shown in Figure 6 for the $x = 1.0$ and 1.3% systems. From our ZF-μSR results in Figure 4, we conclude that the suppression of magnetic ordering is due to a decrease in both the ordered volume fraction and the moment size.

C. Discussion

Our results offer strong evidence that both the ordered moment and fraction are partially or fully suppressed below T_C. The strong suppression of the magnetism below the onset of superconductivity was also observed in the "122" and "11" families of Fe-HTS: $BaFe_{2-x}Co_xAs_2$[10,11] (where re-entrance of the non-AFM phase was reported[15]), $BaFe_{2-x}Ni_xAs_2$[12], $Ba_{1-x}K_xFe_2As_2$[13], and FeSe[32]. However, we note that in $BaFe_{2-x}Co_xAs_2$ and $Ba_{1-x}K_xFe_2As_2$, only the ordered moment decreases below T_C, but the magnetic fraction remains unaffected. Detailed studies of magnetism and superconductivity in the related system $NaFe_{1-x}Co_xAs$ were previously conducted[14]. In $NaFe_{1-x}Co_xAs$, only the ordered moment was diminished below T_C. This reduction is much smaller than that of $NaFe_{1-x}Ni_xAs$. We also noticed that the observed muon precession frequencies in $NaFe_{1-x}Ni_xAs$ and $NaFe_{1-x}Co_xAs$ follow different patterns. We have found two high frequencies and one low frequency for $NaFe_{1-x}Ni_xAs$, while one high frequency and two low frequencies were reported for $NaFe_{1-x}Co_xAs$. Although a definitive explanation for these differences requires further studies, it is clear that Ni and Co dopants perturb the electronic structure of NaFeAs in different ways.

Both the ordered moment and magnetic fraction decrease below T_C for FeSe (which becomes magnetic under hydrostatic pressure). Results in the present investigation of $NaFe_{1-x}Ni_xAs$ are similar to the FeSe case. Itinerant AFM and SC orders are generally expected to compete strongly for the same electronic states; this behavior can be captured within a simple Ginzburg-Landau free energy for the AFM and SC order parameters, $\mathcal{M}$ and Δ, respectively (in the context of Fe-HTS, see for instance Refs. 15, 33–35):

$$F = \frac{a_m}{2}\mathcal{M}^2 + \frac{u_m}{4}\mathcal{M}^4 + \frac{a_s}{2}\Delta^2 + \frac{u_s}{4}\Delta^4 + \frac{\gamma}{2}\mathcal{M}^2\Delta^2$$

The degree of competition between these two orders is encoded in the combination of coefficients $g = \gamma/\sqrt{u_s u_m}$. If the competition is too strong ($g > 1$), these two orders are macroscopically phase separated and do not coexist microscopically. On the other hand, if the competition is weak ($g < 1$), they can establish a coexistence phase in which both order parameters are simultaneously non-zero at the same position. In a homogeneous system, the first scenario is manifested by a reduction of the AFM volume fraction F below T_C without a change in the size of the magnetic moment. Conversely, the second scenario is manifested by a reduction of the magnetic moment below T_C without any variation in the volume fraction. Interestingly, we observe both signatures in $NaFe_{1-x}Ni_xAs$. Although a detailed theoretical analysis is beyond the scope of this work, this suggests that the parameter g itself may be inhomogeneous and change as a function of the position in the sample. If Cooper pairs were to form an unconventional sign-changing $s^{\pm}$ state[36,37], it was argued[15] that the system would be at the verge of phase separation and microscopic coexistence, i.e. $g \approx 1$. In this case, local inhomogeneity could locally alter the value of g in a significant manner[38].

IV. INTERNAL FIELD SIMULATIONS AT MUON STOPPING SITES

To investigate the effect of Ni-dopants on the magnetism in $NaFe_{1-x}Ni_xAs$, we numerically simulate the

behavior of the muon in the magnetic environment of $NaFe_{1-x}Ni_xAs$. In low-temperature μSR experiments, the incident muons thermalize with the lattice and are implanted at interstitial locations referred to as stopping sites. Muon implantation sites in Fe-HTS have been successfully identified using a succession of increasingly accurate theoretical calculations. Early studies were based on the analysis of the local minima of the unperturbed electrostatic potential within either the simple Thomas Fermi or a full Density Functional Theory (DFT) approach. This strategy was specifically followed for the "1111"[17,39–41] and the "11"[32,42] classes of Fe-HTS. In addition, similar calculations were performed on selected "122"[43,44] materials and other systems[45,46]. Recently, and exclusively for the "1111" family of Fe-HTS, the effect of the muon on the lattice was captured within a supercell DFT impurity calculation by considering force and energy relaxations of possible muon implantation sites[47,48].

The ab-initio search often identifies clusters of sites. This is true also in the simple unperturbed potential method, that fails in insulators such as fluorides[49], but yields a correct first approximation in the metallic pnictides owing to the electron screening of the muon charge. In this case, the clusters are defined as the portion of the unit cell volume enclosed by the isosurface corresponding to the muon ground state energy. More accurate stopping site determination would require an impurity DFT approach. Under this methodology, clusters of candidate muon sites are generally found with smaller *intra*-cluster and larger *inter*-cluster energy barriers.

Since muon localization is a metastable epithermal kinetic process that cannot be described by a mere minimum energy criterion, all of these methods uncover clusters of candidate locations that may not directly correspond to observed muon sites. In principle, the true muon fate could be simulated by robust *ab initio* path integral molecular dynamics [50,51]. At present, these techniques are computationally prohibitive for impurity calculations on complex structures such as Fe-HTS. Therefore, the most feasible method for muon site determination in Fe-HTS involves comparing the experimental and calculated local field values at candidate sites.

A. Candidate Muon Stopping Sites in "111" Systems

To determine plausible muon implantation sites in the "111" family of Fe-HTS, we employed DFT methods that account for local crystal deformations and electronic band structure perturbations due to the implanted muons. In particular, muon stopping site calculations in NaFeAs and $NaFe_{1-x}Ni_xAs$ were performed using spin-polarized DFT with plane wave expansions of the Kohn-Sham orbitals at both atomic and interstitial sites. The Generalized Gradient Approximation (GGA) was applied for the exchange correlation functional within the Perdew-Burke Ernzerhof (PBE) formalism[52,53]. Finally, the core wavefunction was approximated using the Projector Augmented Wave (PAW) method[54]. The plane wave and charge density cutoffs were chosen to be 120 and 1080 Ry, respectively. More details on the muon site determination procedure are found in Appendix A 1 and A 2.

This initial search with DFT methods uncovered five plausible muon sites in NaFeAs, which are also assumed to be valid for lowly doped $NaFe_{1-x}Ni_xAs$. The five candidate sites were grouped into two clusters based on relative calculated energies. Since the muon is treated as a classical particle within DFT, corrections due to its light mass can be included by taking into account the spread of the muon wavefunction in the Double Born-Oppenheimer (DBO) approximation method [45]. As described in Appendix A 2, we invoked the DBO approximation to examine the relative stability of the five candidate sites. From our stability checks, we concluded that only two of the three muon sites in the low-energy cluster proved to be stable. In addition, both muon sites in the high-energy cluster relax into each other, suggesting that the muon is likely delocalized between these two sites, which are also in close proximity to each other. As a result, we have determined three plausible muon stopping locations (two stopping sites and a delocalized high-energy stopping position) in NaFeAs, which are listed in Table I.

B. Dipolar Internal Field Simulations on $NaFe_{1-x}Ni_xAs$

With the muon stopping sites determined, magnetic dipolar field simulations were performed by simulating the NaFeAs as an array of localized magnetic dipoles. The two dipolar contributions considered in the internal field simulation are localized electronic moments from AFM-ordered Fe atoms, and random nuclear dipolar moments from all atoms. Non-magnetic nickel impurities were randomly substituted into the Fe sites on the host NaFeAs lattice to generate $NaFe_{1-x}Ni_xAs$. By performing a vector sum of the array of (static) electronic and random nuclear dipolar moments, the internal field distribution was numerically simulated for all points in the crystal.

To capture the stochastic fluctuations in the random nuclear moment directions and Ni site substitutions, the internal field distribution was simulated by performing 10,000 independent trials of dipolar sums for each muon site as a function of Ni concentration x. Although simulated results can be implemented for any x, the simplified dipolar field model severely breaks down beyond $x \gtrsim 0.4\%$ since the simulation does not consider bulk superconductivity (see Figure 1). Magnetic disorder induced by the SC state at $x \gtrsim 0.4\%$ could also explain the disappearance of coherent oscillations in the ZF-μSR spectra in Figure 2. Additional details on the simulation setup for exploring the local magnetic environment at the

$NaFe_{1-x}Ni_xAs$ stopping sites are found in Appendix A 1 and A 3.

C. Discussion of Computational Results

The main results of our computational investigation are summarized in Table I. Our stopping site calculations and stability analysis reveal three plausible muon stopping sites in NaFeAs. This is consistent with the observation that there are three precession frequencies in the ZF-μSR spectra in lightly-doped $NaFe_{1-x}Ni_xAs$. The calculated precession frequencies are listed in Table I, along with the extrapolated frequencies from power law fits of the frequencies from μSR found in Figure 3(a). Moreover, our simulations show that the mean local fields at the two high-field sites make an acute angle of approximately 36° with the crystal c axis, implying that the strong fields at these sites are preferentially aligned with the c axis. This is consistent with our experimental observation that the high frequency oscillations have noticeable amplitudes when the initial muon spin is not aligned with the c axis (i.e. in the spin-rotated configuration), as shown in Figure 2(a). Differences in the simulated and experimentally-obtained angles θ suggest that the true muon sites are likely a small displacement from the ones listed in Table I.

The doping evolution of the simulated precession frequencies are shown in Figure 3(c). Comparisons of the simulated and observed frequencies for Site 1 in our dipolar field simulations enabled us to estimate the ordered moment size of the Fe atoms in NaFeAs to be $\mu_{Fe} = 0.175(3)\mu_B$. The difference between the simulated and experimental frequencies for the second and third sites suggests that quantum correlations (e.g. contact hyperfine fields) contribute to the internal field, which are not included in the dipolar model. In addition, the presence of Ni dopants can perturb the ordering of Fe moments, which was not included in the simulation. Nonetheless, our computational investigation provides a physical interpretation of the frequencies observed in the ZF-μSR spectra and corroborates the model for the magnetic ordering in (1).

The ordered moment size in a variety of Fe-HTS has been explored experimentally using μSR, neutron scattering, and Mössbauer measurements[55]. The reported variations of the ordered Fe moments of the same specimen is a testament to the differences in sensitivity across these three probes of the local moment. Table II shows a comparison of the ordered moment size of representative systems from the various classes of Fe-HTS. The estimate from our present investigation in NaFeAs, $\mu_{Fe} = 0.175(3)\mu_B$, is consistent with the moment sizes reported from neutron scattering[56] and Mössbauer spectroscopy[57].

V. LINEAR RELATIONSHIP BETWEEN ORDERED MOMENT AND T_N

Despite the notable differences in the experimentally-measured ordered moment sizes across different Fe-HTS[55], there are some notable relationships between the ordered moment and other material parameters. The observation of a linear relationship between the muon precession frequency ν and the magnetic ordering temperature T_N was initally noted by Uemura in Ref.[65] for the "122" and "1111" classes of Fe-HTS. Separate linear trends in "122" and "1111" classes of Fe-HTS were discovered from Mössbauer spectroscopy relating the internal hyperfine field and the orthorhombic lattice distortion[10]. The different proportionality constants between the two classes of Fe-HTS have been ascribed to the critical dynamics of the structural and magnetic transitions[66,67]. In this section, we make use of muon stopping site calculations to extend the investigation of the linear trend between the ordered moment size and T_N from μSR results.

A. Linear Trends from μSR Results

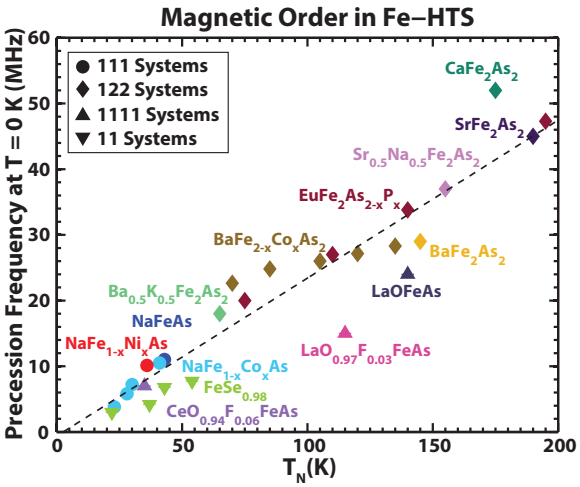

FIG. 7. Correlation between low-temperature muon precession frequency $\nu(T \to 0)$ and the magnetic ordering temperature T_N for various Fe-HTS. The black dashed line is a linear least-squares model of the data. For systems with more than one precession frequency, the maximum frequency is taken. Circle symbols indicate the "111" family of Fe-HTS: NaFeAs[68], $NaFe_{1-x}Co_xAs$[68], and $NaFe_{0.996}Ni_{0.004}As$. Diamond symbols indicate the "122" family of Fe-HTS: $BaFe_2As_2$[65], $Ba_{0.5}K_{0.5}Fe_2As_2$[69], $BaFe_{2-x}Co_xAs_2$[70], $CaFe_2As_2$[16], $EuFe_2As_{2-x}P_x$[71], $SrFe_2As_2$[16], $Sr_{0.5}Na_{0.5}Fe_2As_2$[16]. Upwards-pointing triangle symbols indicate the "1111" family of Fe-HTS: $CaO_{0.94}F_{0.06}FeAs$[65], LaOFeAs[17], $LaO_{0.97}F_{0.03}FeAs$[72]. Downwards-pointing triangle symbols indicate the "11" family of Fe-HTS: $FeSe_{1-x}$[32] under pressure.

TABLE I. Summary of dipolar field simulations in NaFeAs using muon stopping site positions obtained from DFT methods. Similar stopping sites are expected for lightly-doped $NaFe_{1-x}Ni_xAs$. Stopping site positions are given in fractional coordinates. The highest frequency from the dipolar field simulations is in close agreement with the experimental results assuming a static ordered Fe moment of $0.175(3)\mu_B$.

Site	Site Position [a]	Simulated ν (MHz) [b]	Experimental ν (MHz) [c]	Simulated θ (°) [d]	Experimental θ (°) [e]
1	(0.000, 0.875, 0.100)	10.987(49)	10.981(27)	42.1(5)	0(10)
2	(0.100, 0.750, 0.100)	7.839(30)	10.685(57)	31.1(6)	0(10)
3 [f]	(0.500, 0.250, 0.600)	2.090(21)	0.864(06)	0.6(4)	18(10)

[a] Stopping site positions given in fractional coordinates.
[b] Muon precession frequency from dipolar field simulations.
[c] Muon precession frequency from μSR experiments on NaFeAs
[d] Average acute angle between the simulated field direction and the c-axis
[e] Average acute angle between the local field direction and the c-axis. The local field direction was estimated from ZF-μSR measurements with the muon spins rotated in orthogonal directions.
[f] From stability analysis of calculated muon sites, the third frequency is likely attributed to a stopping site delocalized across sites D and E. See Appendix A 2 for more details. For simplicity, we list here the simulated results calculated for site class E from Table IV in Appendix A 2.

TABLE II. Comparison of the low-temperature Fe ordered magnetic moments in selected Fe-HTS. All magnetic moments are given in units of μ_B.

Fe-HTS	μSR	Neutron Scattering	Mössbauer [a]
NaFeAs	0.175(3)	0.17(2)[56]	0.158(2)[57]
$BaFe_2As_2$	0.75(5)[59]	0.87(3)[60]	0.36(4)[61]
LaFeAsO [b]	0.68(2)[39]	0.63(1)[62]	0.34(1)[63]
$FeSe_{0.98}$	0.20(5) [c]	Undetected [d]	0.18(1) [e]

[a] Ordered moment extrapolated from measured low-temperature hyperfine field using the scaling relation 15 T/μ_B[55,58].
[b] Measured at $T \approx 25$ K, above the magnetic ordering temperature of La.
[c] Taken under pressure $p = 2.4$ GPa, from Ref. 32.
[d] No magnetic bragg peaks observed under pressure according to Ref. 32.
[e] FeSe under pressure $p = 2.5$ GPa, from Ref. 64.

Figure 7 depicts the correlation between the low temperature precession frequency $\nu(T \to 0)$ and the ordering temperature T_N for a variety of Fe-HTS, including $NaFe_{1-x}Ni_xAs$ from the present investigation. Note that for the SC samples, the values of the precession frequencies, extrapolated to $T = 0$ from above T_c are taken. Since the precession frequency ν is proportional to the local magnetic field at the muon site, ν is proportional to the ordered moment size, and therefore the magnetization. ν also depends on the distance between the muon stopping site and the dominant ordered moment (Fe atoms). Remarkably, despite the differences in chemical composition and crystal structure across the various main families of Fe-HTS, (which influence the number and location of the muon stopping sites) a linear trend between $\nu(T \to 0)$ and T_N appears to persist. This suggests that the mechanism responsible for driving the magnetic ordering may be similar across different crystal structures and dopant atoms. Under this linear scaling relationship, there is an increase of 0.244(3) MHz/K between the $\nu(T \to 0)$ and T_N.

Since muon stopping sites have been calculated for a variety of Fe-HTS, we can compare the ordered Fe moment sizes directly. The ordered magnetic moment on the Fe atom can be calculated as the scaling factor necessary for matching the precession frequencies from dipolar field simulations against experimental results. Shown in Figure 8 is a comparison between the ordered magnetic moment of the Fe atoms and T_N. A linear model was fit to the data, revealing that the magnetic moment μ_{Fe} scales with T_N as 0.0062(6) μ_B/K across these families of Fe-HTS.

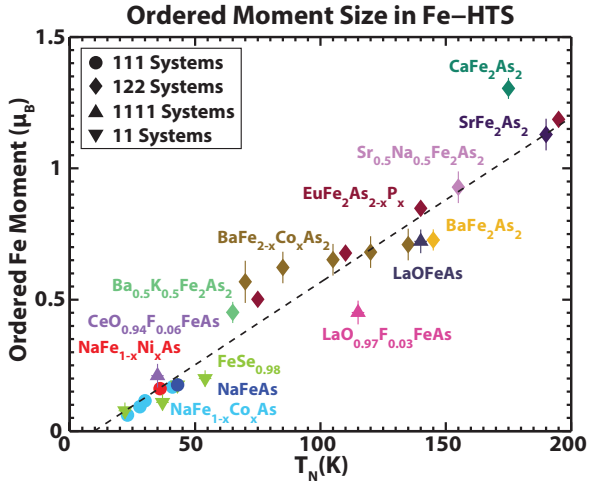

FIG. 8. Correlation between the low-temperature ordered moment size on the Fe atom μ_{Fe} from μSR measurements and the magnetic ordering temperature T_N for various Fe-HTS. The black dashed line is a linear least-squares model of the data. The "111", "122", "1111", and "11" families of Fe-HTS are represented by circle, diamond, upwards-pointing triangle, and downwards-pointing triangle symbols, respectively. See the caption for Figure 7 for references to data points.

B. Discussion

The universal linear relationship between the $T = 0$ sub-lattice magnetization M and the experimentally observed T_N provides important insight into the nature of the magnetic state. Within an itinerant mean-field approach, in which AFM is driven by Fermi surface nesting, $M \propto T_N$ follows naturally whenever the Fermi surfaces are perfectly nested – this is the same relationship between the SC gap function and T_C that appears in BCS theory. Since the Fermi pockets of the iron pnictides are not perfectly nested, it is important to verify whether $M \propto T_N$ applies more generally in itinerant antiferromagnets. To investigate this issue, we consider a widely studied toy model consisting of one circular hole pocket located at the center of the Brillouin zone, and one elliptical electron pocket shifted from the center by the AFM ordering vector[15,33–35,73,74]. The mismatch between the Fermi pockets is tuned by two parameters: δ_2, which characterizes the ellipticity of the electron pocket, and δ_0, which describes the difference between the areas of the Fermi pockets (and is therefore indirectly related to doping). The case $\delta_0 = \delta_2 = 0$ corresponds to perfect nesting, giving $T_{N,0} = (\frac{e^\gamma}{\pi})M_0 \approx 0.567 M_0$.

Following Refs. 15, 33, and 34, we compute not only T_N as a function of the parameters δ_0 and δ_2, but also the magnetization M at $T = 0$. We focus on the regime in which the AFM transition is second order (see Appendix B for details). As shown in Figure 9, M monotonically increases with increasing T_N. Each curve corresponds to a fixed value of δ_2 and continuously changing values of δ_0. Interestingly, when δ_2 is not too large, T_N and M follow a nearly linear relationship over a wide parameter range, which is consistent with previous works[15,33]. Although a quantitative comparison with experimental findings must account for band structure details of different compounds, the results of this simple model are qualitatively consistent with the experimental observations, suggesting that nesting plays an important role in driving the AFM instability.

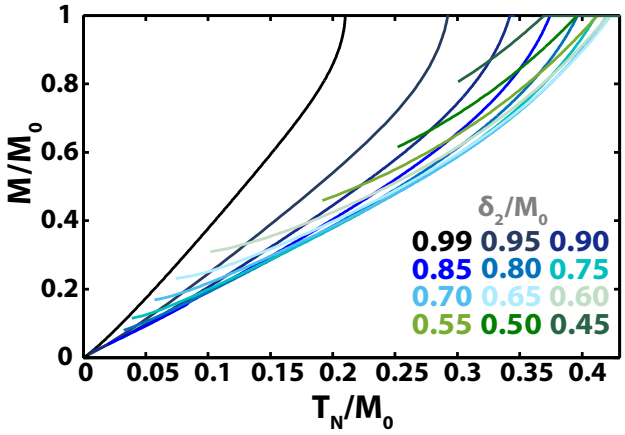

FIG. 9. Theoretical calculations of the ordered moment M at $T = 0$ versus the AFM critical temperature T_N. The ellipticity of the electron band, given by δ_2, is fixed for each curve, whereas the parameter δ_0, corresponding to doping, is varied continuously. M_0 is the AFM moment M at $T = 0$ when the hole and electron Fermi pockets are perfectly nested.

VI. SUPERCONDUCTIVITY IN $NaFe_{1-x}Ni_xAs$

μSR experiments performed with an applied field transverse to the initial muon ensemble spin, called TF-μSR, allow determination of the magnetic field penetration depth λ, which is one of the fundamental parameters of a superconductor[16]. (Recall that λ is related to the superconducting carrier density n_s through $\lambda^{-2} = \mu_0 e^2 n_s/m^*$, where m^* is the effective mass and μ_0 is the vacuum permeability). Most importantly, the temperature dependence of λ is particularly sensitive to the presence of SC nodes. In a fully gapped superconductor, $\Delta\lambda^{-2}(T) \equiv \lambda^{-2}(0) - \lambda^{-2}(T)$ vanishes exponentially at low T and decays as a power of T in a nodal SC. As a result, the μSR technique is a powerful tool to measure λ in type II superconductors. Specifically, μSR experiments in the vortex state of a type II superconductor allow the determination of λ in the bulk of the sample, in contrast to many techniques that probe λ only near the surface.

To understand the temperature evolution of λ, it is informative to study the symmetry and structure of the SC gap. Significant experimental and theoretical efforts have focused on this issue in Fe-HTS[1,2]. However, there is no consensus on a universal gap structure and the relevance for the particular gap symmetry for Fe-HTS, which are the first non-cuprate materials exhibiting superconductivity at relatively high temperatures.

In contrast to cuprates, where the SC gap symmetry is universal, the gap symmetry and/or structure of the Fe-HTS varies across different systems. For instance, nodeless isotropic gap distributions were observed in optimally doped $Ba_{1-x}K_xFe_2As_2$[75,76], $Ba_{1-x}Rb_xFe_2As_2$[29], and $BaFe_{2-x}Ni_xAs_2$[77] as well as in $BaFe_{2-x}Co_xAs_2$[78], $K_xFe_{2-y}Se_2$[79], and $FeTe_{1-x}Se_x$[80,81]. Signatures of nodal SC gaps were reported in LaFePO[82], LiFeP[83], KFe_2As_2[84], $BaFe2(As_{1-x}P_x)_2$[85–88], $BaFe_{2-x}Ru_xAs_2$[89], and FeSe[90] as well as in overdoped $Ba_{1-x}K_xFe_2As_2$[91] and in optimally doped $Ba_{1-x}Rb_xFe_2As_2$ under pressure[92]. Therefore, it is fruitful to extend the study of the SC gap symmetry to other Fe-based materials, specifically the "111" family of Fe-HTS. In this section, we present and discuss TF-μSR results on the $x = 1.3\%$ sample in the superconducting state.

A. TF-μSR Results

Shown in Figure 10 are the TF-μSR time spectra on the $x = 1.3\%$ system, measured in an applied field of 300 Oe above (40 K) and below (2 K) $T_C \approx 15$ K. Above T_C, the oscillations show a small relaxation due to ran-

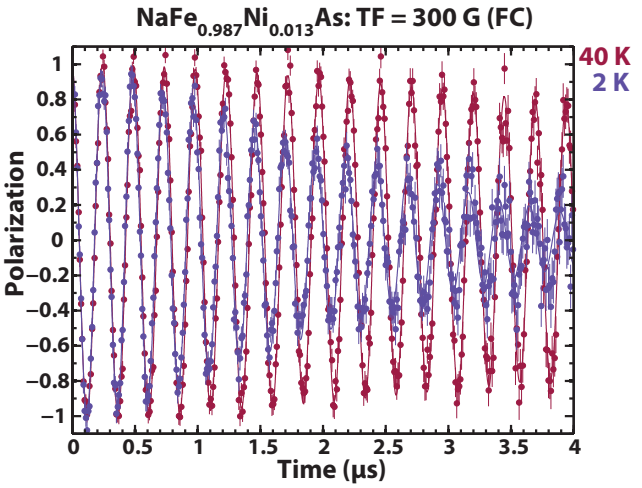

FIG. 10. TF-μSR polarization on field-cooled $x = 1.3\%$ in an applied field of 300 G. Time spectra in the $x = 1.3\%$ system with an applied transverse field at $T = 40$ K (PM) and $T = 2$ K (SC).

dom local fields from nuclear magnetic moments. As the sample is field-cooled below T_C, the relaxation steadily increases due to the presence of a nonuniform local field distribution as a result of the formation of a flux-line lattice (FLL) in the SC state. The TF-μSR spectra were analyzed using the following functional form:

$$P_{\rm TF}(t) = F_{\rm nm}\cos(2\pi\nu t + \phi) \times \exp\left\{-\frac{1}{2}\left(\sigma_{\rm nm}^2 + \sigma_{\rm SC}^2\right)t^2\right\} e^{-\lambda_{\rm Mag}t} \quad (2)$$

The defining parameters in (2) are the precession frequency ν, the relaxation rates $\sigma_{\rm SC}$ and $\sigma_{\rm nm}$ characterizing the damping due to the formation of FLL in the SC state and the nuclear magnetic dipolar contribution, respectively, and an exponential relaxation rate for field-induced magnetism $\lambda_{\rm Mag}$[93]. The model in (2) has been previously used[29,94] for Fe-HTS in the presence of dilute or fast fluctuating electronic moments and it was demonstrated to be sufficiently precise for extracting the SC depolarization rate as a function of temperature.

The temperature dependence of ν shows a PM shift below T_C in Figure 11(a), which is different from the expected diamagnetic shift imposed by the SC state[29,94,95]. It is difficult to elucidate the origin of the PM shift, however the effects are consistent with field-induced magnetism. Other phenomena such as vortex lattice disorder[93] or a Yosida-like decrease of the spin susceptibility[96] may also contribute to this behavior and can be investigated further.

The SC and magnetic relaxation rates, $\sigma_{\rm SC}$ and $\lambda_{\rm Mag}$, respectively, are shown in Figure 11(b)-(c), demonstrating an additional effect of a weak contribution of static magnetism to the SC state. We also observe the non-

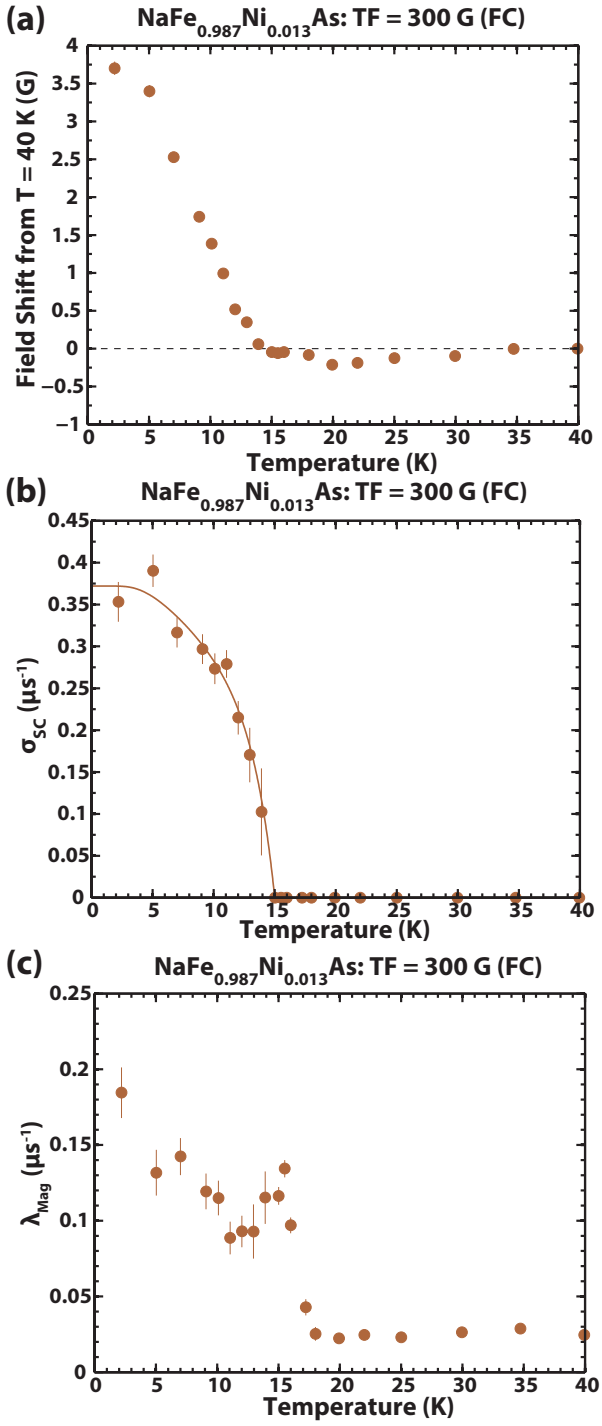

FIG. 11. TF-μSR results on field-cooled $x = 1.3\%$ in an applied field of 300 G. (a) Temperature dependence of the field shift from 40 K (normal state). (b)-(c) Temperature dependences of the relaxation rates ascribed to the SC and magnetic orders, respectively. The solid line in (b) represents an isotropic two-band SC model fit to the temperature evolution of $\sigma_{\rm SC}$. The peak in $\lambda_{\rm Mag}$ in (c) is close to T_C, indicating that the onset of SC order affects the dilute electronic moment distribution.

monotonic temperature dependence of $\lambda_{\rm Mag}$, which may be caused by the interplay between magnetism and superconductivity[15,97]. As the sample is cooled in an external transverse field below $T_{\rm C} \approx 15$ K, $\sigma_{\rm SC}$ begins to rise from 0 due to the FLL formation. $\sigma_{\rm SC}$ saturates upon further cooling, which resembles the behavior of an isotropic nodeless superconductor.

We found that an isotropic two-band (s+s)-wave SC model describes the temperature dependence of the measured $\sigma_{\rm SC}$ remarkably well (see Figure 11(b)), yielding a large gap $\Delta_1 \simeq 4.5(6)$ meV and a small gap $\Delta_2 \simeq 1.8(5)$ meV. Refer to Appendix C for details on the SC gap symmetry analysis. A two-gap scenario is also consistent with the generally accepted view of multi-gap superconductivity in Fe-HTS[1,98]. The magnitudes of the large $2\Delta_1/k_{\rm B}T_{\rm C} \simeq 6.9(5)$ and the small $2\Delta_2/k_{\rm B}T_{\rm C} \simeq 2.8(5)$ gap for $NaFe_{1-x}Ni_xAs$ ($x = 0.013$) are in good agreement with previous work[99]. There it was pointed out that most Fe-HTS exhibit a two-gap SC behavior, characterized by a large gap with magnitude $2\Delta/k_{\rm B}T_{\rm C} \simeq 7(2)$ and a small gap with 2.5(1.5).

B. Connection with Other Unconventional Superconductors

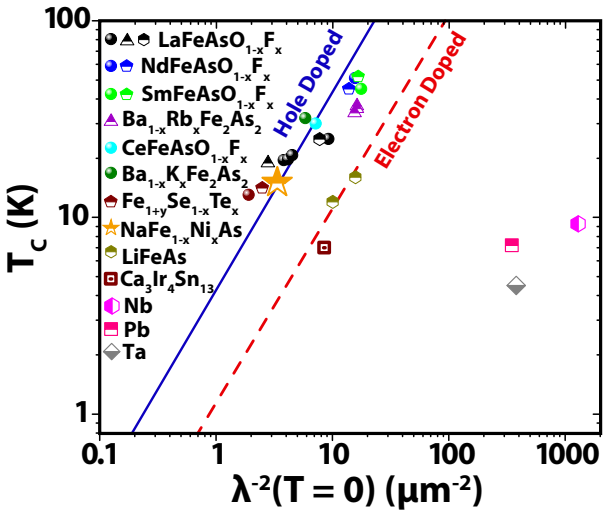

FIG. 12. Uemura plot for hole and electron doped Fe-HTS (see Ref. 100 and references therein). The linear relation observed for underdoped cuprates is shown as a blue colored solid line for hole doping[101,102] and as a red colored dashed line for electron doped systems[103]. The points for conventional BCS superconductors are also shown. The orange star marker shows the data point for $NaFe_{1-x}Ni_xAs$ obtained in this work.

An interesting result of μSR investigations in Fe-HTS is the observed proportionality between $T_{\rm c}$ and the zero-temperature relaxation rate $\sigma(0) \propto \lambda^{-2}(0)$, known as the Uemura plot[101,102]. This relation, which seems to be generic for various families of cuprate HTS, has the features that upon increasing the charge carrier doping $T_{\rm c}$ first increases linearly in the under-doped region (blue line in Figure 12), then saturates, and finally is suppressed for high carrier doping. The initial linear trend of the Uemura relation indicates that for these unconventional HTS, the ratio $T_{\rm C}/E_{\rm F}$ ($E_{\rm F}$ is the Fermi energy) is much larger than that of conventional BCS superconductors. Figure 12 shows $T_{\rm C}$ plotted against $\lambda^{-2}(0)$ for various hole- and electron-doped Fe-HTS (see Ref. 100 and references therein), including the current results on $NaFe_{1-x}Ni_xAs$. The linear relation observed for underdoped cuprates is also shown as a solid line for hole doped cuprates[101,102] and as a dashed line for electron doped cuprates[103]. The present data for $NaFe_{1-x}Ni_xAs$ in the Uemura plot is in close proximity to the line observed in hole-doped cuprates and other Fe-HTS. This connection contrasts with LiFeAs, which shows behavior following electron-doped cuprates. The observation of a reduced superfluid stiffness in $NaFe_{1-x}Ni_xAs$ compared to LiFeAs presents a new challenge for theoretical explanations.

VII. CONCLUSION

In conclusion, the magnetic and SC properties of $NaFe_{1-x}Ni_xAs$ were studied as a function of Ni-content x by DC magnetization and μSR techniques. The long range magnetic order is observed for $x = 0$ and 0.4% samples, while for $x > 0.4\%$ magnetic order becomes inhomogeneous and is completely suppressed for $x = 1.5\%$. The magnetic volume fraction continuously decreases with increasing x. Furthermore, superconductivity acquires its full volume for samples with $x \gtrsim 0.4\%$. This implies that there is a coexistence of magnetism and superconductivity in $NaFe_{1-x}Ni_xAs$. Both the ordered moment and the magnetic volume fraction decrease below $T_{\rm C}$, showing that magnetism, which develops at higher temperatures, becomes partially (or even fully) suppressed by the onset of superconductivity. These results indicate that the competition between the SC and magnetic order parameters in $NaFe_{1-x}Ni_xAs$ develop in an intrinsically inhomogeneous environment, providing important insight for theoretical modeling. A linear relationship between the $T = 0$ ordered moment and the AFM ordering temperature $T_{\rm N}$ for various Fe-HTS is noted, which is consistent with a mean-field approach for itinerant electrons, in which antiferromagnetism is driven by Fermi surface nesting. From TF-μSR measurements, the temperature evolution of the penetration depth in $NaFe_{1-x}Ni_xAs$ is consistent with an isotropic two-gap (s+s)-wave model for superconductivity.

ACKNOWLEDGMENTS

The μSR experiments were performed at TRIUMF in Vancouver, Canada and at the Swiss Muon Source

(SμS) at Paul Scherrer Insitute (PSI) in Villigen, Switzerland. The authors sincerely thank the TRIUMF Center for Material and Molecular Science staff and the PSI Bulk μSR Group for invaluable technical support with μSR experiments. Work at the Department of Physics of Columbia University is supported by US NSF DMR-1436095 (DMREF) and NSF DMR-1610633. Z. Guguchia gratefully acknowledges the financial support by the Swiss National Science Foundation (SNF fellowships P2ZHP2-161980 and P300P2-177832). Work at Columbia, TRIUMF, PSI and IOP-Beijing has been supported by the REIMEI project funding from the Japan Atomic Energy Agency, and by the support from the Friends of Tokyo University Inc (FUTI). E.M. is supported by CNPq (grant number 304311/2010-3). P.B. acknowledges computing resources provided by STFC Scientific Computing Department's SCARF cluster. R.D.R. acknowledges funding by the European Unions Horizon 2020 research and innovation programme under grant agreement No 654000. This work was supported by the computational node hours granted from the Swiss National Supercomputing Centre (CSCS) under project ID sm07. R.M.F. is supported by the U.S. Department of Energy, Office of Science, Basic Energy Sciences, under Award number DE-SC0012336. C.D.C. acknowledges financial support by the National Natural Science Foundation of China Grant No. 51471135, the National Key Research and Development Program of China under contract No. 2016YFB1100101, and Shaanxi International Cooperation Program. Works at IOPCAS are supported by NSF and MOST of China through Research Projects as well as by CAS External Cooperation Program of BIC (112111KYS820150017). The present work is a part of the Ph.D. thesis of S.C.C. submitted to and defended at Columbia University in August 2017.

Appendix A: Internal Field Simulation

1. Initialization of Crystal Properties

At low temperatures, NaFeAs crystallizes into the Cmme space group, with the following assumed lattice constants for the orthorhombic structure based on Ref. 19: $a = 5.6834$ Å, $b = 5.6223$ Å, and $c = 6.9063$ Å. Stopping site calculations and subsequent dipolar field calculations were performed on $NaFe_{1-x}Ni_xAs$ with the atomic properties displayed in Table III. The sample was assumed to be in the low temperature ordered state with Fe spins aligned in the usual colinear AFM arrangement as depicted in Figure 1(d).

2. Muon Stopping Site Determination

The search for muon sites was initiated by sampling a $4 \times 4 \times 4$ grid of possible interstitial positions in the NaFeAs lattice that are at least 1 Å away from lattice atoms. Symmetry-equivalent points in the search grid were removed with the spacegroup symmetry of the lattice. The stability of a H atom in a $2 \times 2 \times 2$ supercell consisting of 96 Na-Fe-As atoms was examined at each point in the grid. A $2 \times 2 \times 2$ Monkhorst-Pack grid of $\vec{k}$-points was used for Brillouin zone sampling. DFT calculations were carried out assuming the usual collinear magnetic ordering of Fe atoms in NaFeAs as shown in Figure 1(d)[19]. To accommodate for structural relaxations, the forces were optimized till a threshold of 10^{-3} atomic units and the energies till a threshold of 10^{-4} atomic units. Table IV lists five candidate muon sites for NaFeAs using this first-order search procedure. These sites are also assumed to be compatible for lowly doped $NaFe_{1-x}Ni_xAs$.

TABLE III. Summary of crystal parameters for low-temperature simulations of $NaFe_{1-x}Ni_xAs$.

Atom	Sym.	Position [a]	Nuc. Mom. [b]	Mag. Mom. [c]
Na	4g	(0.000, 0.250, 0.651)	2.217	–
Fe	4a	(0.250, 0.000, 0.000)	0.091	0.175
Ni	–	Fe-substitution	-0.750	–
As	4g	(0.000, 0.250, 0.198)	1.439	–

[a] Atomic positions given in fractional coordinates.
[b] Nuclear moments given in units of μ_N.
[c] Ordered magnetic moments given in units of μ_B.

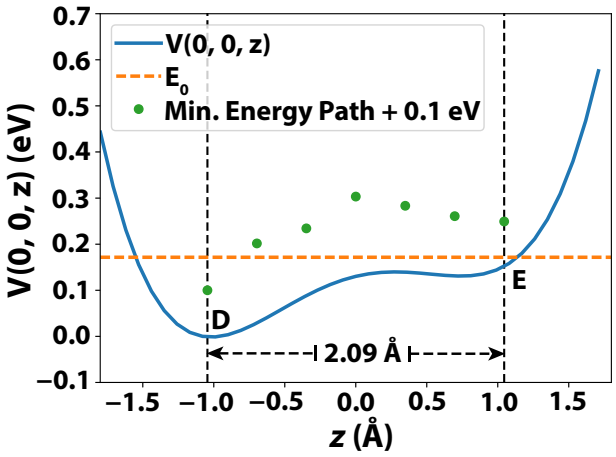

FIG. 13. A toy model potential $V(0, 0, z)$ (solid line) together with the ground state energy, $E_0 = 0.17$ eV from solving the Schrödinger equation for a muon in a potential of the form $V(x, y, z) = \frac{1}{2}a(x^2 + y^2) + \frac{1}{2}(bz^4 - cz^2 + dz) + f$ with $a = 2.44\times10^{-3}$, $b = 5.04\times10^{-4}$, $c = 3\times10^{-3}$, $d = 2.85\times10^{-3}$, and $f = 4.79 \times 10^{-3}$, all in Hartree atomic units. The green dots show the minimum energy profile map from the DBO for the symmetric site D to site E. These simulations imply that the muon is likely delocalized over the two sites in Cluster II (sites D and E).

TABLE IV. Summary of candidate muon stopping sites in NaFeAs determined by DFT. Muon site locations are believed to be similar for $NaFe_{1-x}Ni_xAs$. The local magnetic field strength $|\vec{B}|$ is nearly constant for each particular muon site position, confirming that the majority of the local field comes from the ordered Fe moments. The static ordered Fe moment was set to $\mu_{Fe} = 0.175(3)\mu_B$ to match the high frequency in the experimental spectra.

Cluster	Label	Symmetry	Site Position [a]	ΔE (meV) [b]	Field $\|\vec{B}\|$ (G) [c]	Frequency ν (MHz) [d]	Angle θ (°) [e]
I	A	8n	(0.100, 0.750, 0.100)	0	578.5(2.1)	7.839(30)	42.1(5)
I	B	8m	(0.000, 0.875, 0.100)	42	810.9(3.5)	10.987(49)	31.1(6)
I	C	8l	(0.250, 0.500, 0.250)	183	488.3(4.1)	6.616(56)	88.6(4)
II	D	4b	(0.750, 0.500, 0.500)	287	1.002(69)	0.014(40)	0.2(3)
II	E	4g	(0.500, 0.250, 0.600)	436	154.2(1.5)	2.090(21)	0.6(4)

[a] Candidate muon stopping site positions given in fractional coordinates.
[b] DFT total energy difference from stopping site A
[c] Magnetic field at muon site from dipolar field simulations
[d] Simulated muon precession frequency
[e] Average acute angle between the simulated field direction and the c-axis

We group the five candidate sites into two clusters based on stability checks using the Double Born-Oppenheimer approximation method (DBO)[45], which takes into account the quantum description of the muon. Within this method, a potential exploration algorithm (PEA) is used to efficiently sample the a priori unknown potential felt by the muon. With the sampling of the potential, site C is observed to be a local minimum in the muon potential. Site C relaxes towards sites A and B since site C has very low barrier less than 0.24 eV that is too small to bind the muon. Sites A and B are also close in proximity to each other and in energy difference. Consequently, we associate sites A, B, and C together as Cluster I. Similarly, we also observe that sites E and D relaxes into each other, which together form Cluster II. Our clustering also explains the observed frequencies - Cluster I contains the low DFT energy sites that describe the high muon field observed from experiment, while Cluster II contains sites that correspond to the low field.

Shown in Figure 13 are the results of further analysis of the sites in Cluster II. The energy profile extracted from the DBO potential map can be represented by the toy model shown in Figure 13. This enables us to solve the Schrödinger equation of the muon, yielding a ground state energy of 0.17 eV (independent of the interpolation method and the boundary condition, to some extent) which is greater than the barrier seen in the potential map. These findings suggest that the muon wavefunction for the low field sites may be delocalized over positions between sites D and E (hereafter the D-E site). As a result, the low frequency detected from experiments may come from an averaging of the field at the two sites. Following analysis considering the quantum nature of the muon due to its light mass, we propose that sites A, B and D-E are the possible implantation sites of the muon.

DBO would still predict a zero average at the D-E sites probed by the muon wavefunction due to the symmetry of the sites in the lattice. However a DFT mapping of the total energy and a separate solution of the muon Schrödinger equation may not give the final answer, since the muon quantum nature is ignored in the DFT assessment of the total energy. The actual muon site may still be slightly distorting the local environment, thus justifying the small but nonvanishing low precession frequency listed in Table I.

3. Low Temperature Dipolar Field Simulation

A $9 \times 9 \times 9$ supercell of magnetic dipoles was used to model the internal field of $NaFe_{1-x}Ni_xAs$. Dipole positions and strengths for the idealized crystal structure in NaFeAs listed in Table III. Nuclear dipole moment directions are assumed to be random for all atoms while the spins on Fe are assumed to take on a collinear AFM striped pattern, common to other Fe-HTS. To simulate the effect of doping, the magnetic Fe atoms are randomly substituted with nonmagnetic Ni atoms to achieve the desired Ni concentration x. The dipolar field at the muon site was obtained by summing over all dipoles in the $NaFe_{1-x}Ni_xAs$ supercell.

By comparing the simulated frequencies, shown in Table IV, with the experimental results, we can associate the two high frequencies ν_1 and ν_2 with sites B and A, respectively. The low frequency ν_3 corresponds best with site E of Cluster II. However, our stability analysis shows that the muon is likely delocalized over sites D and E. A comparison between simulated and experimental results is presented in Table I. Our simulations show that the experimentally observed frequency $\nu_1 = 10.9$ MHz in NaFeAs corresponds to an ordered Fe moment size of about $\mu_{Fe} = 0.175(3)\mu_B$.

Appendix B: Ordered Moment Scaling Calculations

In this section, we present a description of the two-band model discussed in Section V and introduced in Refs. 33 and 34. The effective free energy density of the

model can be written as

$$f = \frac{2\mathcal{M}^2}{I} - \frac{T}{\upsilon}\sum_{\omega_n}\sum_{\boldsymbol{k}} \ln[(\omega_n^2 + E_{+,\boldsymbol{k}}^2)(\omega_n^2 + E_{-,\boldsymbol{k}}^2)] \quad \text{(B1)}$$

where $\mathcal{M}$ is the temperature dependent ordered AFM moment, $I > 0$ is the AFM interaction coupling constant, $\omega_n = 2\pi T(n + 1/2)$ is a fermionic Matsubara frequency ($n \in \mathbb{Z}$), υ is the volume of the system, and

$$E_{\pm,\boldsymbol{k}} = \sqrt{\mathcal{M}^2 + \xi_k^2} \pm |\delta_\theta|.$$

Here, $\xi_k = k^2/2m - \epsilon_0$ is a parabolic energy dispersion, θ is the angle in the Fermi surface between the momentum $\boldsymbol{k}$ and the x-axis, and $\delta_\theta \equiv \delta_0 + \delta_2\cos(2\theta)$ describes deviations from the perfect nesting condition.

The momentum sum can be evaluated as $\frac{1}{\upsilon}\sum_{\boldsymbol{k}} \to \frac{m}{2\pi}\int_{-\infty}^{\infty} \mathrm{d}\xi \int_0^{2\pi} \frac{\mathrm{d}\theta}{2\pi}$. We minimize f in (B1) with respect to $\mathcal{M}$ and perform the $\mathrm{d}\xi$ integration to obtain

$$\frac{\mathcal{M}}{mI} = T\sum_{0<\omega_n<\Lambda} \int \frac{\mathrm{d}\theta}{2\pi}\,\mathrm{Re}\,\frac{\mathcal{M}}{\sqrt{\mathcal{M}^2 + (\omega_n + i|\delta_\theta|)^2}}, \quad \text{(B2)}$$

where Λ is a high-frequency cutoff. At $T = 0$, we integrated over frequencies to obtain

$$\mathrm{Re}\int \frac{\mathrm{d}\theta}{2\pi} \ln\left(i|\delta_\theta| + \sqrt{M^2 - \delta_\theta^2}\right) = \ln M_0, \quad \text{(B3)}$$

where $M \equiv \mathcal{M}(T = 0)$ and $M_0 \equiv 2\Lambda e^{-2\pi/mI}$ is the value of M for $\delta_0 = 0 = \delta_2$.

When the transition is second order, T_N is the temperature at which $\mathcal{M}(T \to T_\mathrm{N}) \to 0$. Setting $\mathcal{M} = 0$ in (B2) and performing the Matsubara sum yields

$$2\ln\left(\frac{4\pi T_\mathrm{N}}{M_0}\right) + \int \frac{\mathrm{d}\theta}{2\pi}\left[\psi\left(\frac{1}{2} + \frac{i\delta_\theta}{2\pi T_\mathrm{N}}\right) + \psi\left(\frac{1}{2} - \frac{i\delta_\theta}{2\pi T_\mathrm{N}}\right)\right] = 0 \quad \text{(B4)}$$

where $\psi(z) \equiv \frac{\mathrm{d}}{\mathrm{d}z}\ln\Gamma(z)$ is the digamma function.

We have numerically calculated the remaining angular integral in the self-consistent equations (B3) and (B4) to determine the behavior of M and T_N as functions of δ_0 and δ_2. For fixed δ_2, the transition is second order at small δ_0 but becomes first order at larger δ_0. Moreover, there is no ordered AFM state[34] for $\delta_2 > M_0$. On the other hand, the ordered magnetic moment at $T = 0$ generally increases with decreasing δ_0 and δ_2 and abruptly saturates at $\delta_0 + \delta_2 = M_0$. These results are presented in Fig. 14. More importantly, these results enable us to plot and examine the behavior of the ordered moment at $T = 0$ vs. T_N, which is shown in Fig. 9.

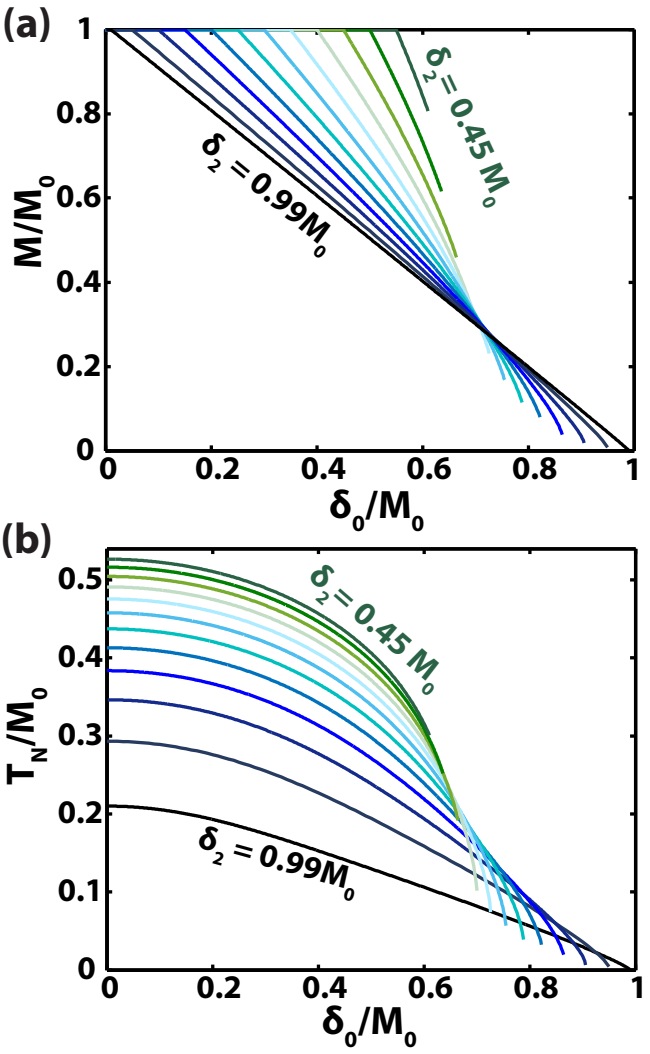

FIG. 14. Summary of numerical results for the ordered moment M and T_N. (a) Ordered moment M at $T = 0$ and (b) T_N as functions of the area difference parameter δ_0 for fixed values of the ellipticity parameter δ_2. Results are shown in the regime where the transition is second order. Colors represent different values of δ_2/M_0 listed in Figure 9.

Appendix C: TF-μSR SC Gap Analysis

To explore the SC gap symmetry, we recall that the penetration depth $\lambda(T)$ (in an isotropic superconductor) is related to the quadratic relaxation rate $\sigma_\mathrm{SC}(T)$ through $\sigma_\mathrm{SC}(T) = k\gamma_\mu\Phi_0\lambda^{-2}(T)$, where γ_μ is the muon gryomagnetic ratio, $\Phi_0 \equiv \frac{h}{2e}$ is the quantum of magnetic flux, and $k \approx 0.06091$ is a geometric factor characterizing the FLL[25,104]. The temperature evolution of $\lambda(T)$ can be modeled for a variety of SC gap symmetries and structures.

Within the local London limit of electrodynamics (where the penetration depth λ is much greater than the SC coherence length ξ), the α-model is a popular phenomenological framework used to study multiband superconductivity[105–107]. The α-model assumes that the SC gaps in different bands are independent from each other (aside from sharing a common T_C) and that the normalized penetration depth $\frac{\lambda(T)}{\lambda(0)}$ follows the same tempera-

ture dependence as in the single-band clean-limit BCS theory. A two-band α-model in which the superfluid densities from each band are added together was used to analyze the TF-μSR results:

$$\frac{\sigma_{\rm SC}(T)}{\sigma_{\rm SC}(0)} = \sum_{j=1}^{2} f_j \frac{\lambda^{-2}(T,\tilde{\Delta}_j)}{\lambda^{-2}(0,\tilde{\Delta}_j)} \qquad \text{(C1)}$$

where $\tilde{\Delta}_j$ is the maximum value of the SC gap at $T = 0$ for each band ($j = 1, 2$). The relative contributions from each band is imposed through the constraint $\sum_{j=1}^{2} f_j = 1$ in (C1).

Assuming that the Fermi velocity is constant in magnitude, the penetration depth is determined through the integral expression[108]:

$$\frac{\lambda^{-2}(T,\tilde{\Delta}_j)}{\lambda^{-2}(0,\tilde{\Delta}_j)} = 1 + \frac{1}{\pi}\int_0^{2\pi} \mathrm{d}\varphi \int_{\tilde{\Delta}_j}^{\infty} E\,\mathrm{d}E \times \cdots \left(\frac{\partial f}{\partial E}\right) \frac{1}{\sqrt{E^2 - \Delta_j^2(T,\varphi)}} \qquad \text{(C2)}$$

where $f(E) \equiv [1+\exp(E/k_{\rm B}T)]^{-1}$ is the Fermi function. The SC gap functions $\Delta_j(T,\varphi)$ in (C2) are assumed to have the separable form: $\Delta_j(T,\varphi) = \tilde{\Delta}_j g(\frac{T}{T_{\rm C}}) S(\varphi)$. The temperature dependence of the gap is approximated by the function $g(t) = \tanh[\alpha(\beta(t^{-1}-1)^{\delta})]$, with $\alpha = 1.82$, $\beta = 1.018$, and $\delta = 0.51$[108]. The SC gap symmetry is embedded in $S(\varphi)$, which is defined to be 1 for s-wave and (s+s)-wave gaps and $|\cos(2\varphi)|$ for d-wave gaps.

The results of applying (C1) to the $x = 1.3\%$ system are shown in Figure 11(b), demonstrating that the two-band α-model with an (s+s)-wave SC gap is a feasible model for the data.

---

* These authors contributed equally to this work.
† tomo@lorentz.phys.columbia.edu

1 G. R. Stewart, Rev. Mod. Phys. **83**, 1589 (2011).
2 D. J. Scalapino, Rev. Mod. Phys. **84**, 1383 (2012).
3 P. Dai, Rev. Mod. Phys. **87**, 855 (2015).
4 E. P. Rosenthal, E. F. Andrade, C. J. Arguello, R. M. Fernandes, L. Y. Xing, X. C. Wang, C. Q. Jin, A. J. Millis, and A. N. Pasupathy, Nature Physics **10**, 225 (2014).
5 Y. J. Uemura, Nat Mater **8**, 253 (2009).
6 M. Yi, D. Lu, J.-H. Chu, J. G. Analytis, A. P. Sorini, A. F. Kemper, B. Moritz, S.-K. Mo, R. G. Moore, M. Hashimoto, W.-S. Lee, Z. Hussain, T. P. Devereaux, I. R. Fisher, and Z.-X. Shen, Proceedings of the National Academy of Sciences **108**, 6878 (2011).
7 R. M. Fernandes, A. V. Chubukov, and J. Schmalian, Nature Physics **10**, 97 (2014).
8 J.-H. Chu, J. G. Analytis, K. De Greve, P. L. McMahon, Z. Islam, Y. Yamamoto, and I. R. Fisher, Science **329**, 824 (2010).
9 S. Nandi, M. G. Kim, A. Kreyssig, R. M. Fernandes, D. K. Pratt, A. Thaler, N. Ni, S. L. Bud'ko, P. C. Canfield, J. Schmalian, R. J. McQueeney, and A. I. Goldman, Phys. Rev. Lett. **104**, 057006 (2010).
10 T. Goltz, V. Zinth, D. Johrendt, H. Rosner, G. Pascua, H. Luetkens, P. Materne, and H.-H. Klauss, Phys. Rev. B **89**, 144511 (2014).
11 D. W. Tam, Y. Song, H. Man, S. C. Cheung, Z. Yin, X. Lu, W. Wang, B. A. Frandsen, L. Liu, Z. Gong, T. U. Ito, Y. Cai, M. N. Wilson, S. Guo, K. Koshiishi, W. Tian, B. Hitti, A. Ivanov, Y. Zhao, J. W. Lynn, G. M. Luke, T. Berlijn, T. A. Maier, Y. J. Uemura, and P. Dai, Phys. Rev. B **95**, 060505 (2017).
12 C. J. Arguello, *Scanning Tunneling Microscopy Studies of Charge Density Waves in $NbSe_2$ and μSR studies of Nickel doping in $BaFe_2As_2$*, Ph.D. thesis, Columbia University (2014).
13 E. Wiesenmayer, H. Luetkens, G. Pascua, R. Khasanov, A. Amato, H. Potts, B. Banusch, H.-H. Klauss, and D. Johrendt, Phys. Rev. Lett. **107**, 237001 (2011).
14 J. D. Wright, T. Lancaster, I. Franke, A. J. Steele, J. S. Möller, M. J. Pitcher, A. J. Corkett, D. R. Parker, D. G. Free, F. L. Pratt, P. J. Baker, S. J. Clarke, and S. J. Blundell, Phys. Rev. B **85**, 054503 (2012).
15 R. M. Fernandes, D. K. Pratt, W. Tian, J. Zarestky, A. Kreyssig, S. Nandi, M. G. Kim, A. Thaler, N. Ni, P. C. Canfield, R. J. McQueeney, J. Schmalian, and A. I. Goldman, Phys. Rev. B **81**, 140501 (2010).
16 T. Goko, A. A. Aczel, E. Baggio-Saitovitch, S. L. Bud'ko, P. C. Canfield, J. P. Carlo, G. F. Chen, P. Dai, A. C. Hamann, W. Z. Hu, H. Kageyama, G. M. Luke, J. L. Luo, B. Nachumi, N. Ni, D. Reznik, D. R. Sanchez-Candela, A. T. Savici, K. J. Sikes, N. L. Wang, C. R. Wiebe, T. J. Williams, T. Yamamoto, W. Yu, and Y. J. Uemura, Phys. Rev. B **80**, 024508 (2009).
17 H. Luetkens, H.-H. Klauss, M. Kraken, F. J. Litterst, T. Dellmann, R. Klingeler, C. Hess, R. Khasanov, A. Amato, C. Baines, M. Kosmala, O. J. Schumann, M. Braden, J. Hamann-Borrero, N. Leps, A. Kondrat, G. Behr, J. Werner, and B. Buchner, Nature Materials **8**, 305 (2009).
18 W. Wang, Y. Song, C. Cao, Y. Li, L. Harriger, W. Tian, R. Yu, A. H. Nevidomskyy, and P. Dai, (Submitted 2016).
19 S. Li, C. de la Cruz, Q. Huang, G. F. Chen, T.-L. Xia, J. L. Luo, N. L. Wang, and P. Dai, Phys. Rev. B **80**, 020504 (2009).
20 K. Momma and F. Izumi, Journal of Applied Crystallography **44**, 1272 (2011).
21 M. A. Tanatar, N. Spyrison, K. Cho, E. C. Blomberg, G. Tan, P. Dai, C. Zhang, and R. Prozorov, Phys. Rev. B **85**, 014510 (2012).
22 D. R. Parker, M. J. P. Smith, T. Lancaster, A. J. Steele, I. Franke, P. J. Baker, F. L. Pratt, M. J. Pitcher, S. J. Blundell, and S. J. Clarke, Phys. Rev. Lett. **104**, 057007

(2010).
[23] A. F. Wang, X. G. Luo, Y. J. Yan, J. J. Ying, Z. J. Xiang, G. J. Ye, P. Cheng, Z. Y. Li, W. J. Hu, and X. H. Chen, Phys. Rev. B **85**, 224521 (2012).
[24] A. F. Wang, J. J. Lin, P. Cheng, G. J. Ye, F. Chen, J. Q. Ma, X. F. Lu, B. Lei, X. G. Luo, and X. H. Chen, Phys. Rev. B **88**, 094516 (2013).
[25] A. Yaouanc and P. D. de Réotier, *Muon Spin Rotation, Relaxation, and Resonance: Applications to Condensed Matter*, 1st ed., International Series of Monographs on Physics, Vol. 147 (Oxford University Press, 2010).
[26] A. Schenck, *Muon Spin Rotation Spectroscopy: Principles and Applications in Solid State Physics*, 1st ed. (Adam Hilger, Bristol, 1985).
[27] S. Lee, S. Kilcoyne, and R. Cywinski, *Muon Science: Muons in Physics, Chemistry and Materials*, 1st ed., Scottish Graduate Series, Vol. 51 (CRC Press, 1999).
[28] A. Suter and B. Wojek, Physics Procedia **30**, 69 (2012).
[29] Z. Guguchia, R. Khasanov, Z. Bukowski, F. von Rohr, M. Medarde, P. K. Biswas, H. Luetkens, A. Amato, and E. Morenzoni, Phys. Rev. B **93**, 094513 (2016).
[30] T. Goko, C. J. Arguello, A. Hamann, T. Wolf, M. Lee, D. Reznik, A. Maisuradze, R. Khasanov, E. Morenzoni, and Y. J. Uemura, npj Quantum Materials **2**, 44 (2017).
[31] Y. J. Uemura, Hyperfine Interactions **49**, 205 (1989).
[32] M. Bendele, A. Ichsanow, Y. Pashkevich, L. Keller, T. Strässle, A. Gusev, E. Pomjakushina, K. Conder, R. Khasanov, and H. Keller, Phys. Rev. B **85**, 064517 (2012).
[33] R. M. Fernandes and J. Schmalian, Phys. Rev. B **82**, 014521 (2010).
[34] A. B. Vorontsov, M. G. Vavilov, and A. V. Chubukov, Phys. Rev. B **81**, 174538 (2010).
[35] D. E. Almeida, R. M. Fernandes, and E. Miranda, Phys. Rev. B **96**, 014514 (2017).
[36] P. J. Hirschfeld, M. M. Korshunov, and I. I. Mazin, Reports on Progress in Physics **74**, 124508 (2011).
[37] A. V. Chubukov, D. V. Efremov, and I. Eremin, Phys. Rev. B **78**, 134512 (2008).
[38] M. Hoyer, S. V. Syzranov, and J. Schmalian, Phys. Rev. B **89**, 214504 (2014).
[39] R. D. Renzi, P. Bonfá, M. Mazzani, S. Sanna, G. Prando, P. Carretta, R. Khasanov, A. Amato, H. Luetkens, M. Bendele, F. Bernardini, S. Massidda, A. Palenzona, M. Tropeano, and M. Vignolo, Superconductor Science and Technology **25**, 084009 (2012).
[40] G. Prando, P. Bonfà, G. Profeta, R. Khasanov, F. Bernardini, M. Mazzani, E. M. Brüning, A. Pal, V. P. S. Awana, H.-J. Grafe, B. Büchner, R. De Renzi, P. Carretta, and S. Sanna, Phys. Rev. B **87**, 064401 (2013).
[41] H. Maeter, H. Luetkens, Y. G. Pashkevich, A. Kwadrin, R. Khasanov, A. Amato, A. A. Gusev, K. V. Lamonova, D. A. Chervinskii, R. Klingeler, C. Hess, G. Behr, B. Büchner, and H.-H. Klauss, Phys. Rev. B **80**, 094524 (2009).
[42] R. Khasanov, Z. Guguchia, A. Amato, E. Morenzoni, X. Dong, F. Zhou, and Z. Zhao, Phys. Rev. B **95**, 180504 (2017).
[43] J. Sugiyama, H. Nozaki, I. Umegaki, M. Harada, Y. Higuchi, K. Miwa, E. J. Ansaldo, J. H. Brewer, M. Imai, C. Michioka, K. Yoshimura, and M. Månsson, Phys. Rev. B **91**, 144423 (2015).
[44] Z. Shermadini, *Iron based pnictide and chalcogenide superconductors studied by muon spin spectroscopy*, Ph.D. thesis, Technische Universitt Dresden (2014).
[45] P. Bonfá, F. Sartori, and R. De Renzi, The Journal of Physical Chemistry C **119**, 4278 (2015).
[46] N. Adam, E. Suprayoga, B. Adiperdana, H. Guo, H. Tanida, S. S. Mohd-Tajudin, R. Kobayashi, M. Sera, T. Nishioka, M. Matsumura, S. Sulaiman, M. I. Mohamed-Ibrahim, and I. Watanabe, Journal of Physics: Conference Series **551**, 012053 (2014).
[47] J. S. Möller, P. Bonfá, D. Ceresoli, F. Bernardini, S. J. Blundell, T. Lancaster, R. D. Renzi, N. Marzari, I. Watanabe, S. Sulaiman, and M. I. Mohamed-Ibrahim, Physica Scripta **88**, 068510 (2013).
[48] P. Bonfá and R. D. Renzi, Journal of the Physical Society of Japan **85**, 091014 (2016).
[49] F. Bernardini, P. Bonfà, S. Massidda, and R. De Renzi, Phys. Rev. B **87**, 115148 (2013).
[50] D. Marx and M. Parrinello, The Journal of Chemical Physics **104**, 4077 (1996).
[51] T. Miyake, T. Ogitsu, and S. Tsuneyuki, Phys. Rev. Lett. **81**, 1873 (1998).
[52] J. P. Perdew and Y. Wang, Phys. Rev. B **45**, 13244 (1992).
[53] J. P. Perdew, K. Burke, and M. Ernzerhof, Phys. Rev. Lett. **77**, 3865 (1996).
[54] P. E. Blöchl, Phys. Rev. B **50**, 17953 (1994).
[55] M. D. Lumsden and A. D. Christianson, Journal of Physics: Condensed Matter **22**, 203203 (2010).
[56] G. Tan, Y. Song, C. Zhang, L. Lin, Z. Xu, T. Hou, W. Tian, H. Cao, S. Li, S. Feng, and P. Dai, Phys. Rev. B **94**, 014509 (2016).
[57] I. Presniakov, I. Morozov, A. Sobolev, M. Roslova, A. Boltalin, V. Son, O. Volkova, A. Vasiliev, S. Wurmehl, and B. Bchner, Journal of Physics: Condensed Matter **25**, 346003 (2013).
[58] D. Vij, *Handbook of Applied Solid State Spectroscopy* (Springer, 2006).
[59] B. P. P. Mallett, Y. G. Pashkevich, A. Gusev, T. Wolf, and C. Bernhard, EPL (Europhysics Letters) **111**, 57001 (2015).
[60] Q. Huang, Y. Qiu, W. Bao, M. A. Green, J. W. Lynn, Y. C. Gasparovic, T. Wu, G. Wu, and X. H. Chen, Phys. Rev. Lett. **101**, 257003 (2008).
[61] M. Rotter, M. Tegel, D. Johrendt, I. Schellenberg, W. Hermes, and R. Pöttgen, Phys. Rev. B **78**, 020503 (2008).
[62] N. Qureshi, Y. Drees, J. Werner, S. Wurmehl, C. Hess, R. Klingeler, B. Büchner, M. T. Fernández-Díaz, and M. Braden, Phys. Rev. B **82**, 184521 (2010).
[63] M. A. McGuire, R. P. Hermann, A. S. Sefat, B. C. Sales, R. Jin, D. Mandrus, F. Grandjean, and G. J. Long, New Journal of Physics **11**, 025011 (2009).
[64] K. Kothapalli, A. E. Bhmer, W. T. Jayasekara, B. G. Ueland, P. Das, A. Sapkota, V. Taufour, Y. Xiao, E. Alp, S. L. Budko, P. C. Canfield, A. Kreyssig, and A. I. Goldman, Nature Communications **7**, 12728 (2016).
[65] Y. Uemura, Physica B: Condensed Matter **404**, 3195 (2009), proceedings of the International Conference on Strongly Correlated Electron Systems.
[66] S. D. Wilson, C. R. Rotundu, Z. Yamani, P. N. Valdivia, B. Freelon, E. Bourret-Courchesne, and R. J. Birgeneau, Phys. Rev. B **81**, 014501 (2010).
[67] A. Cano, M. Civelli, I. Eremin, and I. Paul, Phys. Rev. B **82**, 020408 (2010).
[68] D. R. Parker, M. J. Pitcher, P. J. Baker, I. Franke, T. Lancaster, S. J. Blundell, and S. J. Clarke, Chem. Commun.

, 2189 (2009).

[69] A. A. Aczel, E. Baggio-Saitovitch, S. L. Budko, P. C. Canfield, J. P. Carlo, G. F. Chen, P. Dai, T. Goko, W. Z. Hu, G. M. Luke, J. L. Luo, N. Ni, D. R. Sanchez-Candela, F. F. Tafti, N. L. Wang, T. J. Williams, W. Yu, and Y. J. Uemura, Phys. Rev. B **78**, 214503 (2008).

[70] C. Bernhard, C. N. Wang, L. Nuccio, L. Schulz, O. Zaharko, J. Larsen, C. Aristizabal, M. Willis, A. J. Drew, G. D. Varma, T. Wolf, and C. Niedermayer, Phys. Rev. B **86**, 184509 (2012).

[71] Z. Guguchia, A. Shengelaya, A. Maisuradze, L. Howald, Z. Bukowski, M. Chikovani, H. Luetkens, S. Katrych, J. Karpinski, and H. Keller, Journal of Superconductivity and Novel Magnetism **26**, 285 (2013).

[72] J. P. Carlo, Y. J. Uemura, T. Goko, G. J. MacDougall, J. A. Rodriguez, W. Yu, G. M. Luke, P. Dai, N. Shannon, S. Miyasaka, S. Suzuki, S. Tajima, G. F. Chen, W. Z. Hu, J. L. Luo, and N. L. Wang, Phys. Rev. Lett. **102**, 087001 (2009).

[73] J. Knolle, I. Eremin, A. V. Chubukov, and R. Moessner, Phys. Rev. B **81**, 140506 (2010).

[74] R. M. Fernandes, A. V. Chubukov, J. Knolle, I. Eremin, and J. Schmalian, Phys. Rev. B **85**, 024534 (2012).

[75] H. Ding, P. Richard, K. Nakayama, K. Sugawara, T. Arakane, Y. Sekiba, A. Takayama, S. Souma, T. Sato, T. Takahashi, Z. Wang, X. Dai, Z. Fang, G. F. Chen, J. L. Luo, and N. L. Wang, EPL (Europhysics Letters) **83**, 47001 (2008).

[76] R. Khasanov, D. V. Evtushinsky, A. Amato, H.-H. Klauss, H. Luetkens, C. Niedermayer, B. Büchner, G. L. Sun, C. T. Lin, J. T. Park, D. S. Inosov, and V. Hinkov, Phys. Rev. Lett. **102**, 187005 (2009).

[77] M. Abdel-Hafiez, Y. Zhang, Z. He, J. Zhao, C. Bergmann, C. Krellner, C.-G. Duan, X. Lu, H. Luo, P. Dai, and X.-J. Chen, Phys. Rev. B **91**, 024510 (2015).

[78] K. Terashima, Y. Sekiba, J. H. Bowen, K. Nakayama, T. Kawahara, T. Sato, P. Richard, Y.-M. Xu, L. J. Li, G. H. Cao, Z.-A. Xu, H. Ding, and T. Takahashi, Proceedings of the National Academy of Sciences **106**, 7330 (2009).

[79] Y. Zhang, L. X. Yang, M. Xu, Z. R. Ye, F. Chen, C. He, H. C. Xu, J. Jiang, B. P. Xie, J. J. Ying, X. F. Wang, X. H. Chen, J. P. Hu, M. Matsunami, S. Kimura, and D. L. Feng, Nat Mater **10**, 273 (2011).

[80] H. Miao, P. Richard, Y. Tanaka, K. Nakayama, T. Qian, K. Umezawa, T. Sato, Y.-M. Xu, Y. B. Shi, N. Xu, X.-P. Wang, P. Zhang, H.-B. Yang, Z.-J. Xu, J. S. Wen, G.-D. Gu, X. Dai, J.-P. Hu, T. Takahashi, and H. Ding, Phys. Rev. B **85**, 094506 (2012).

[81] P. K. Biswas, G. Balakrishnan, D. M. Paul, C. V. Tomy, M. R. Lees, and A. D. Hillier, Phys. Rev. B **81**, 092510 (2010).

[82] J. D. Fletcher, A. Serafin, L. Malone, J. G. Analytis, J.-H. Chu, A. S. Erickson, I. R. Fisher, and A. Carrington, Phys. Rev. Lett. **102**, 147001 (2009).

[83] K. Hashimoto, S. Kasahara, R. Katsumata, Y. Mizukami, M. Yamashita, H. Ikeda, T. Terashima, A. Carrington, Y. Matsuda, and T. Shibauchi, Phys. Rev. Lett. **108**, 047003 (2012).

[84] J. K. Dong, S. Y. Zhou, T. Y. Guan, H. Zhang, Y. F. Dai, X. Qiu, X. F. Wang, Y. He, X. H. Chen, and S. Y. Li, Phys. Rev. Lett. **104**, 087005 (2010).

[85] K. Hashimoto, M. Yamashita, S. Kasahara, Y. Senshu, N. Nakata, S. Tonegawa, K. Ikada, A. Serafin, A. Carrington, T. Terashima, H. Ikeda, T. Shibauchi, and Y. Matsuda, Phys. Rev. B **81**, 220501 (2010).

[86] M. Yamashita, Y. Senshu, T. Shibauchi, S. Kasahara, K. Hashimoto, D. Watanabe, H. Ikeda, T. Terashima, I. Vekhter, A. B. Vorontsov, and Y. Matsuda, Phys. Rev. B **84**, 060507 (2011).

[87] Y. Nakai, T. Iye, S. Kitagawa, K. Ishida, S. Kasahara, T. Shibauchi, Y. Matsuda, and T. Terashima, Phys. Rev. B **81**, 020503 (2010).

[88] Y. Zhang, Z. R. Ye, Q. Q. Ge, F. Chen, J. Jiang, M. Xu, B. P. Xie, and D. L. Feng, Nat Phys **8**, 371 (2012).

[89] X. Qiu, S. Y. Zhou, H. Zhang, B. Y. Pan, X. C. Hong, Y. F. Dai, M. J. Eom, J. S. Kim, Z. R. Ye, Y. Zhang, D. L. Feng, and S. Y. Li, Phys. Rev. X **2**, 011010 (2012).

[90] C.-L. Song, Y.-L. Wang, P. Cheng, Y.-P. Jiang, W. Li, T. Zhang, Z. Li, K. He, L. Wang, J.-F. Jia, H.-H. Hung, C. Wu, X. Ma, X. Chen, and Q.-K. Xue, Science **332**, 1410 (2011).

[91] J. S. Kim, G. R. Stewart, Y. Liu, and T. A. Lograsso, Phys. Rev. B **91**, 214506 (2015).

[92] Z. Guguchia, A. Amato, J. Kang, H. Luetkens, P. K. Biswas, G. Prando, F. von Rohr, Z. Bukowski, A. Shengelaya, H. Keller, E. Morenzoni, R. M. Fernandes, and R. Khasanov, Nature Communications **6**, 8863 (2015).

[93] J. E. Sonier, W. Huang, C. V. Kaiser, C. Cochrane, V. Pacradouni, S. A. Sabok-Sayr, M. D. Lumsden, B. C. Sales, M. A. McGuire, A. S. Sefat, and D. Mandrus, Phys. Rev. Lett. **106**, 127002 (2011).

[94] R. Khasanov, A. Maisuradze, H. Maeter, A. Kwadrin, H. Luetkens, A. Amato, W. Schnelle, H. Rosner, A. Leithe-Jasper, and H.-H. Klauss, Phys. Rev. Lett. **103**, 067010 (2009).

[95] T. J. Williams, A. A. Aczel, E. Baggio-Saitovitch, S. L. Bud'ko, P. C. Canfield, J. P. Carlo, T. Goko, H. Kageyama, A. Kitada, J. Munevar, N. Ni, S. R. Saha, K. Kirschenbaum, J. Paglione, D. R. Sanchez-Candela, Y. J. Uemura, and G. M. Luke, Phys. Rev. B **82**, 094512 (2010).

[96] K. Yosida, Phys. Rev. **110**, 769 (1958).

[97] J. Kang, X. Wang, A. V. Chubukov, and R. M. Fernandes, Phys. Rev. B **91**, 121104 (2015).

[98] P. J. Hirschfeld, M. M. Korshunov, and I. I. Mazin, Reports on Progress in Physics **74**, 124508 (2011).

[99] D. V. Evtushinsky, D. S. Inosov, V. B. Zabolotnyy, M. S. Viazovska, R. Khasanov, A. Amato, H.-H. Klauss, H. Luetkens, C. Niedermayer, G. L. Sun, V. Hinkov, C. T. Lin, A. Varykhalov, A. Koitzsch, M. Knupfer, B. Bchner, A. A. Kordyuk, and S. V. Borisenko, New Journal of Physics **11**, 055069 (2009).

[100] Z. Guguchia, F. v. Rohr, Z. Shermadini, A. T. Lee, S. Banerjee, A. R. Wieteska, C. A. Marianetti, H. Luetkens, Z. Gong, B. A. Frandsen, S. C. Cheung, C. Baines, A. Shengelaya, A. N. Pasupathy, E. Morenzoni, S. J. L. Billinge, A. Amato, R. J. Cava, R. Khasanov, and Y. J. Uemura, Nature Communications **8**, 1082 (2017).

[101] Y. J. Uemura, G. M. Luke, B. J. Sternlieb, J. H. Brewer, J. F. Carolan, W. N. Hardy, R. Kadono, J. R. Kempton, R. F. Kiefl, S. R. Kreitzman, P. Mulhern, T. M. Riseman, D. L. Williams, B. X. Yang, S. Uchida, H. Takagi, J. Gopalakrishnan, A. W. Sleight, M. A. Subramanian, C. L. Chien, M. Z. Cieplak, G. Xiao, V. Y. Lee, B. W. Statt, C. E. Stronach, W. J. Kossler, and X. H. Yu, Phys. Rev. Lett. **62**, 2317 (1989).

[102] Y. J. Uemura, A. Keren, L. P. Le, G. M. Luke, B. J.

Sternlieb, W. D. Wu, J. H. Brewer, R. L. Whetten, S. M. Huang, S. Lin, R. B. Kaner, F. Diederich, S. Donovan, G. Gruner, and K. Holczer, Nature **352**, 605 (1991).
[103] A. Shengelaya, R. Khasanov, D. G. Eshchenko, D. Di Castro, I. M. Savić, M. S. Park, K. H. Kim, S.-I. Lee, K. A. Müller, and H. Keller, Phys. Rev. Lett. **94**, 127001 (2005).
[104] E. H. Brandt, Phys. Rev. B **37**, 2349 (1988).
[105] H. Padamsee, J. E. Neighbor, and C. A. Shiffman, Journal of Low Temperature Physics **12**, 387 (1973).
[106] O. V. Dolgov, R. K. Kremer, J. Kortus, A. A. Golubov, and S. V. Shulga, Phys. Rev. B **72**, 024504 (2005).
[107] D. C. Johnston, Superconductor Science and Technology **26**, 115011 (2013).
[108] A. Carrington and F. Manzano, Physica C: Superconductivity **385**, 205 (2003).